UNIVERSITY of CALIFORNIA
SANTA CRUZ

THE STELLAR WIND INGESTING LUMINOSITY OF MASSIVE BLACK HOLES IN THE LOCAL UNIVERSE

A thesis submitted in partial satisfaction of the
requirements for the degree of

BACHELOR OF SCIENCE

in

PHYSICS

by

Ricardo Fernandez Jr.

9 June 2011

The thesis of Ricardo Fernandez Jr. is approved by:

Professor Enrico Ramirez-Ruiz
Advisor

Professor Adriane Steinacker
Theses Coordinator

Professor David P. Belanger
Chair, Department of Physics

Abstract

The Stellar Wind Ingesting Luminosity of Massive Black Holes in the Local Universe

by

Ricardo Fernandez Jr.

The nuclei of some galaxies undergo violent activity, quasars being the most extreme instances of this phenomenon. Such activity is short-lived compared to galactic lifetimes, and was more prevalent when the Universe was only about one-fifth of its present age. The growth of a black hole, with the mass of millions, or even billions, of suns is the inevitable end point of such activity, and dead quasars (massive black holes now starved of fuel, and therefore quiescent) should be more common than active quasars and are now being discovered in nearby galaxies and (less convincingly) in the nuclei of globular clusters. But before accepting this conclusion, we must ask a further question: can a black hole lurk in these quiescent galaxies and globular cluster nuclei without showing other evidence for its presence? We are used to the idea that black holes are implicated in the most powerful sources in the universe, and can (when accreting) be ultra efficient radiators. So could a black hole be so completely starved of fuel that it does not reveal its presence?

Such central black holes become detectable only through interactions with its environment. We do not directly know how much gas there is near a massive black hole, and there is no a priori reason why this region should be swept clean of gas. The star density, however, is much better known after all, if the stars were not closely packed near the center of the galaxy or globular cluster nuclei, we would not have evidence for the central black hole at all. Gas that is lost from nearby stars into such black holes should produce a detectable signature.

The steady luminosity resulting from stellar wind feeding, whose intensity depends on the concentration of stars enclosed in the black hole's sphere of influence as well as the rates and velocity of the mass injection, could thus be the clearest diagnostic of a black hole's presence. The question at the forefront of my attention is: *what are the feeding rates supply to massive black holes due solely to the ingestion of winds from neighboring stars?* The answer to this question is derived by means of hydrodynamic simulations, which are used here to model the accretion luminosity of a central massive black hole accreting off the winds of the surrounding stellar members. The code framework developed here assumes the distribution of mass and energy input by stellar winds is spherically symmetry. Such an assumption, allowed me to include the gravitational potential of both the black hole and the cluster. In particular, I use my numerical formalism to model the Galactic center with its central massive black hole and the globular cluster G1 and its is highly debated central black hole. In additionally I outline my plans to extending and improving my numerical formalism to include a better treatment of feedback (by the black hole) and cooling processes.

Contents

To my parents and Dominica for their never ending

love and support.

Acknowledgements

I would like to thank my advisor Professor Enrico Ramirez-Ruiz for his support, guidance, and his contagious love for the sciences. I would like to thank Dr. Bruce Schumm and Dr. Jason Nielsen for their guidance and wonderful courses. Lastly, I would like to thank Jill Naiman for her support and encouragement.

1

Introduction

Black holes have captured the popular imagination in an unprecedented way. Invisible by definition, their existence has proved difficult to substantiate. A black hole is a region of space from which no material objects, light or signal of any kind can escape. It was first suggested in 1783 by John Michell and again in 1798 by Pierre Laplace, that in our universe there might exist objects that would be invisible because the force of gravity at the surface would be so large that it would not allow light to escape it. Over a hundred years later Einstein published his reformulation of the theory of gravitation and shortly thereafter Karl Schwarzschild, while serving in the German Army on the Russian front, derived a general solution for the gravitational field surrounding a spherical mass. Schwarzschilds solution bared the objects first enunciated by Michell and Laplace, that for a given star of mass there is a critical radius (now called the Schwarzschilds radius) such that if the stars mass were compressed to this critical radius it would forever trap the emitted light from surface of the star. Schwarzschild's implications were met with skepticism by most theorist of that time, including Einstein himself. However, the spark was ignited and during the

following decades many great theoretical physicists joined the quest for understanding these fascinating objects.

Black holes are no longer the desolate objects envisioned by Michell and Laplace. On the contrary they are lively, interacting with gas, shredding and engulfing stars. In fact, today we believe super-massive black holes ($M \sim 10^6 - 10^{10} M_\odot$) lurk at the centres of most galaxies (Kormendy & Richstone 1995; Magorrian et al. 1998; Ferrarese & Ford 2005). Their evolution is deeply linked to the evolution of their residing galaxy. Moreover, a new class of black holes have emerged on the scene called intermediate mass black holes ($M \sim 10^2 - 10^5 M_\odot$), thought to reside at the centres of star clusters. Their importance entails the dynamics of stellar clusters, the formation of super-massive black holes, and the production and detection of gravitational waves. It is undeniable, that searching and understanding black holes is vital for understanding the cosmos. In this thesis I focus on the properties exhibit by massive black holes (massive meaning non-stellar) when fed by stellar winds. In the following sections I briefly overview massive black holes and their demographics in galactic nuclei, introduce the recently accumulated evidence for massive black holes in star clusters, and finally discuss the feeding of such massive black holes by stellar winds.

1.1 Brief History of Massive Black Holes in Galactic Nuclei

The honor of the most powerful, steady, high-energy sources in the cosmos belongs to the thousands (or probably millions) of active galactic nuclei (AGNs) sprinkled throughout our universe (Melia 2009). The first hint of their presence was established in the early 1960's when radio astronomers identified them as point like sources. Optical ob-

servations showed that these objects looked like stars (see Figure 1.1) but their spectrum was unlike any star known. Caltech astronomer Maarten Schmidt made the discovery that

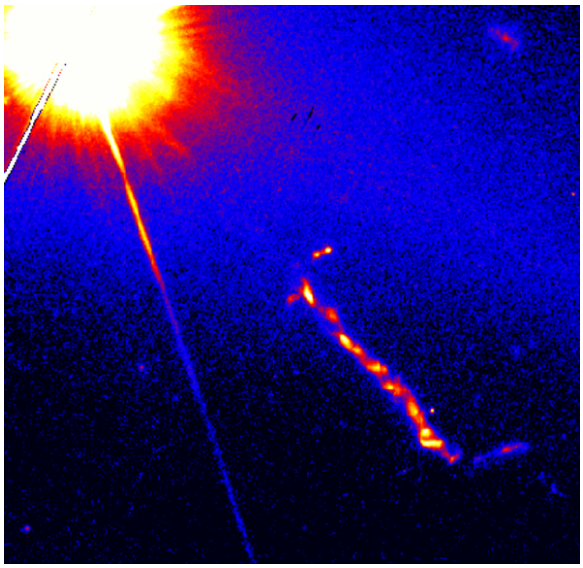

Figure 1.1: Optical image of the quasar 3C273 as observed by the Hubble Space Telescope. Credit: NASA/STSci

these sources were expanding at a considerable fraction of the speed of light (Thorne 1994). Such a high velocity would mean these objects were very far away in our Universe, a natural consequence of its expansion in accordance with Hubble's law. Due to the enormous distances, nearly the largest ever recorded at that time, AGNs had to radiate with an enormous amount of power, hundred times or more than the most luminous galaxies ever seen (Thorne 1994).

A new question then arose: what are the engines that power AGNs? Many ideas were proposed such as supermassive stars, giant pulsars, bursts of star formation that make multiple supernova explosions, and super-massive black holes (SMBHs). Over time SMBHs have become the general consensus (Ho et al. 2000). The key arguments that led to the

acceptance of MBH as central engines are as follows.

Many AGNs vary in brightness in time-scales as short as days, hours, or even minutes (Ferrarese & Ford 2005). This implies the energy source of the AGNs must be very compact due to the fact that a source of light cannot vary on a time-scale shorter than the time it takes for light to traverse the source's diameter. So from the onset, a compact and efficient engine was required. The most commonly discussed mechanism at that time was nuclear energy, which was responsible for powering stars. In 1969 Donald Lynden-Bell, a British astrophysicist at Cambridge, set out to calculate the nuclear power produced by AGNs. To his astonishment he found nuclear reactions alone is implausible, "Evidently although our aim was to produce a model based on nuclear fuel, we have ended up with a model which has produced more than enough energy by gravitational contraction. The nuclear fuel has ended as an irrelevance." Further, deep gravitational potentials have long been inferred from the large velocity widths of the emission lines from nearby gas seen at optical and ultraviolet wavelengths (Ho et al. 2000). Lastly, observations show that many AGN jets are well collimated and straight over mega-parsec scales (see Figure 1.2). The natural explanation is a single rotating black hole that acts like a gyroscope and launches a jet in a fixed direction (Melia 2009).

Through the tireless work of many scientists, we now generally believe that AGNs are powered by SMBHs. Their enormous energy output are due to accretion of gas onto the SMBH from their local environment. Interestingly, SMBHs were concocted to explain AGNs before there was any direct evidence of their existence. Naturally, finding and understanding SMBHs has become one of the holly grails of astronomy.

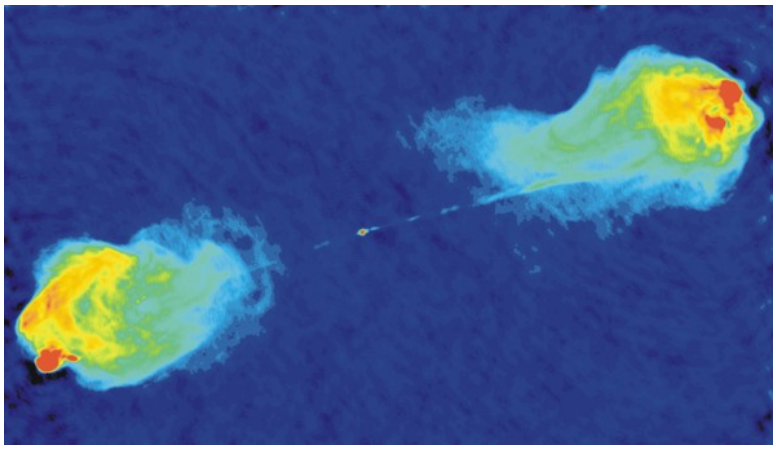

Figure 1.2: Radio image of the radio jet lobes in Cygnus A. Credit: NRAO/AUI

1.2 AGN Demography

Several billion years after the big bang, the Universe went through a quasar era when high-power AGNs were more than 10,000 times as numerous as they are now (Kormendy et al. 2001). High-power AGNs must then have been a common occurrence in most large galaxies. During this era it is believed that a significant fraction of the mass in SMBHs was assembled (Soltan 1982; Yu & Tremaine 2002), due to the large amounts of gas available for accretion onto the black hole. Such gas was made available due to interactions and mergers (see Figure 1.3) between galaxies which are known to trigger large-scale nuclear gas inflows (Hernquist 1989; Barnes & Hernquist 1992).

Since then, the AGN population has mostly died out and thus there should be many SMBHs starved of fuel hiding in nearby galaxies (Kormendy et al. 2001). Therefore, our search for these objects need not to be confined to their earlier glorious past but also to their current quiescent state.

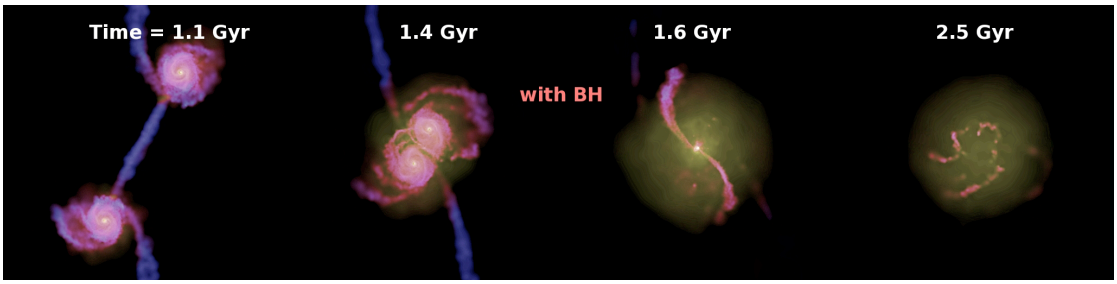

Figure 1.3: Snapshots of the simulated time evolution of the merging of two galaxies with a black hole. The merging leads to large amounts of gas available for accretion by the black hole–reproduced from Di Matteo et al. (2005).

1.3 Massive Black Holes in Globular Clusters

For the past century astronomers have been accustomed to the idea that black holes come in two sizes, small (stellar black hole), and extra large (super massive black hole). Although there has been a wealth of supporting evidence for the existence of stellar and SMBHs, the evidence for black holes of intermediate mass (i.e. $10^3 - 10^5 M_\odot$) is less certain. A natural question then arises: do black holes of intermediate mass exist?

Over the last few years, four lines of evidence have accumulated pointing to the possible presence of an intermediate mass black hole (IMBH) in some highly concentrated collection of stars, usually referred to as globular clusters:

- The first hint is due to the relationship between the mass of the SMBH and the spheroid luminosity of the host galaxy, $M_{\rm BH} - M_{\rm Bulge}$ relation. Extrapolation of the this relationship leads to the prediction of IMBHs in globular clusters (Kormendy & Richstone 1995).

- The second hint stems from the discovery of a new class of objects called ultra luminous x-ray sources (ULXs). It has been suggested that these objects are IMBHs due to their

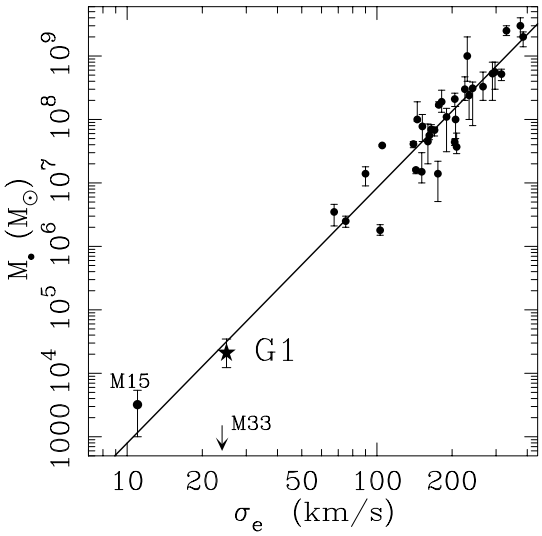

Figure 1.4: The $M - \sigma$ relation for nearby by galaxies which has the IMBH mass estimate for the globular cluster M15 and G1 overlaid the linear fit–reproduced from Gebhardt et al. (2002).

high luminosity and variability, rather than binaries containing stellar black holes, and they are more likely to occur in young star clusters (Zezas et al. 2002).

- The third hint emanates from the analysis of the central velocity dispersions of specific globular clusters. The analysis conducted by Gerssen et al. (2002, 2003) and Gebhardt et al. (2002) of the globular clusters M15 and G1 have resulted to the predictions IMBHs of masses $M \sim 10^3 M_\odot$ and $M \sim 10^4 M_\odot$ respectively (see Figure 1.4).

- Finally the N-body simulations performed by Portegies Zwart et al. (2004) of the evolution of the cluster MGG 11 in the starburst galaxy M82. Their simulations showed that the dynamical friction leads to massive stars sinking rapidly to the center of the cluster, where they participate in a runaway collision, which ultimately collapses to an IMBH of $M \sim 10^3 M_\odot$. Since these cluster may resemble globular clusters in

their youth, it is most probable that at least some globular cluster harbor IMBHs.

None of the four hints presented bear enough weight alone to be convincing. However, the fact that the arguments are so different in nature, we cannot deny the possibility of the existence of IMBHs. The question then arises: how can we tell which globular clusters contain IMBHs?

1.4 Feeding Massive Black Holes by Stellar Winds

The sections that follow have been motivated by the following question: how can we detect massive black holes (MBHs)? Even though SMBHs and IMBHs live in different environments, they have a common trait, both are surrounded by stars. These same stars should provide mass outflows, whose strength depends on the age of the surrounding stellar population. Initially, the stellar winds collide with each other and the surrounding interstellar medium, creating hot shocked stellar winds that fill up the nearby region. At long enough times (a few sound crossing times), a flow can be established in which mass is slowly funnelled to the massive black hole. This flow depends on the concentration of stars enclosed in the black hole's sphere of influence as well as the rates and velocity of the mass injection by the stellar winds. Such a flow would create an accretion luminosity signaling the presence of a MBH, and in fact should be a defining characteristic of MBH with stellar cusps. Therefore the feeding rates of MBHs are ultimately connected with the detections of quiescent MBHs. Thus the question I address in this thesis is: what are the feeding rates of MBHs due solely to the ingestion of winds from neighboring stars?

We explore this question by means of hydrodynamic simulations, which are used to model the accretion luminosity of a central MBH accreting off the winds of the surrounding

stellar members. Our code models the distribution of mass and energy input by stellar winds assuming spherical symmetry. Such an assumption, allowed me to include the gravitational potential of both the MBH and the cluster. In particular, I use my numerical formalism to model the Galactic center with its central SMBH and the globular cluster G1 and its is highly debated central IMBH. In additionally I outline my plans to extending and improving my numerical formalism to include a better treatment of feedback (by the MBH) and cooling.

2

Computational Gas Dynamics: Methods and Algorithms

2.1 Hydrodynamics

The calculation of feeding rates from MBHs due solely to the ingestion of winds from neighboring stars, demands a detailed treatment of the shocked gas. Such a treatment, is entailed by the equations governing fluid flows, which are the discipline of Hydrodynamics. The backbone governing the description of fluid flows are the conservation laws. Conservation demands that mass, momentum, and energy are never created nor destroyed but only redistributed or converted (excluding mass) from one form to another. Further, we employ the equation of state, which describes the nature and the type of gas. The three conservation laws and the equation of state are collectively known as the Euler equations when expressed in a fixed coordinate system.

The Euler equations for compressible, inviscid (free viscosity), and in the presence

of a gravitational field in one, two, or three dimensions are

$$\frac{\partial \rho}{\partial t} + \nabla \cdot (\rho\, \vec{v}) = 0, \qquad \text{(Continuity Equation)} \tag{2.1}$$

$$\frac{\partial \rho \vec{v}}{\partial t} + \nabla \cdot \rho \vec{v}\vec{v} = -\nabla p + \rho \vec{g}, \qquad \text{(Momentum Equation)} \tag{2.2}$$

$$\frac{\partial\, (\rho E)}{\partial t} + \nabla \cdot (\rho E)\, \vec{v} = \rho \vec{v} \cdot \vec{g}, \qquad \text{(Energy Equation)} \tag{2.3}$$

where ρ is the fluid density, $\vec{v}$ is the velocity, p is the pressure, $\vec{g}$ is the acceleration due to gravity, t is the time, and finally, E is the total energy per unit mass. The energy E consists of two parts, the internal energy ϵ and the kinetic energy per unit mass

$$E = \epsilon + \frac{1}{2} v^2. \tag{2.4}$$

At this point we have five equations, two from the energy and continuity and three from the momentum equation, but we have six unknowns (ρ, v_x, v_y, v_z, ϵ and p). In order to make any meaningful predictions of the fluid flow we need to close the set of equations (the number of unknowns equal to the number of equations). This is accomplished by the equation of state which is a manifestations of the conservation laws on the microscopic level. The equation of state depends on the nature of the fluid. In the simplest case, the ideal gas law can be invoked

$$p = (\gamma - 1)\, \rho \epsilon, \tag{2.5}$$

where γ is the ratio of specific heats.

2.2 Computational Eulerian Hydrodynamics

In the preceding section we introduced the equations that describe the evolution of a fluid. Due to the complexity of the Euler equations, analytical solutions are seldom

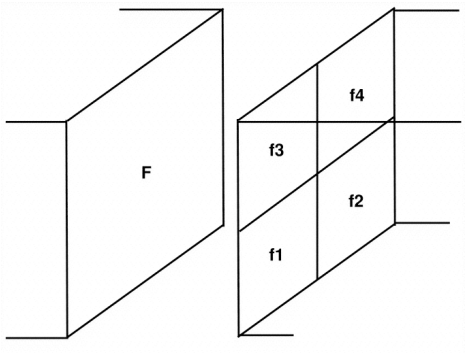

Figure 2.1: The flux F at the left interface must equal the four fluxes labeled f1, f2, f3, and f4 at the right of the interface, F=f1+f2+f3+f4–reproduced from Fryxell et al. (2000).

available for only the most highly idealized problems. Therefore, we will have to resort to numerical computational methods.

Roughly speaking, we divide the computational domain into cells; the cells need not to have the same volume. At each cell the flow variables are assumed to be constant, thus, at each interface of adjoining cells we have uniform initial conditions except for a single jump discontinuity. This feature along with the Euler equations is called the Riemann problem for which exists an exact analytical solution. This treatment permits the calculation of sharp shock fronts and contact discontinuities without introducing significant non-physical oscillations into the flow. Thus, the flow variables are advanced in time by the conservation of mass, momentum, and energy at each interface (see Figure 2.1).

Although our treatment here assumes the flow variables constant in each cell, this method is limited to first-order accuracy in space and time. Second order accuracy in both space and time can be achieved by representing the flow variables as piecewise linear instead of piecewise constant functions. This is analogous when one switches from the rectangle rule to the trapezoid rule in numerical integration of a function. Taking the analogy further,

when one switches from the trapezoid rule to Simpson's rule, the next natural step is to switch from piecewise linear to piecewise parabolic functions. This is commonly called the piecewise parabolic method (PPM). This method naturally allows jump discontinuities to occur anywhere, making them ideal for shocks. Of course the PPM cost more to build, evaluate, and requires more storage space than the constant or linear piecewise functions. Nevertheless, for discontinuous functions and the accuracy improvements, PPM easily justifies the additional costs.

2.3 FLASH & Adaptive Mesh Refinement

As alluded to in the earlier section, we will resort to a numerical approach to solve the Euler equations. The numerical package chosen for this task is FLASH version 3.2. FLASH is a hydrodynamical code that solves the Euler equations for compressible fluid flows in three-dimensions. FLASH was developed by the Center for Astrophysical Thermonuclear Flashes, or FLASH center, at the University of Chicago. The mission of the center is to significantly advance the understanding of problems related to thermonuclear flashes on the surfaces and in the interiors of compact stars (neutron stars and white dwarfs). These problems demand a variety of different phenomena such as accretion flow onto the surface of a compact star, shear flow, Rayleigh-Taylor instabilities on the stellar surface, ignition of nuclear burning, equations of state for relativistic and degenerate matter, and radiation hydrodynamics. In order to treat such a wide scope of processes, the FLASH center developed a flexible code that allows users to tailor it for a given problem.

In numerical simulations, often the phenomena of interest happens at scales much smaller than the computational domain. To resolve many of these small scale phenomena

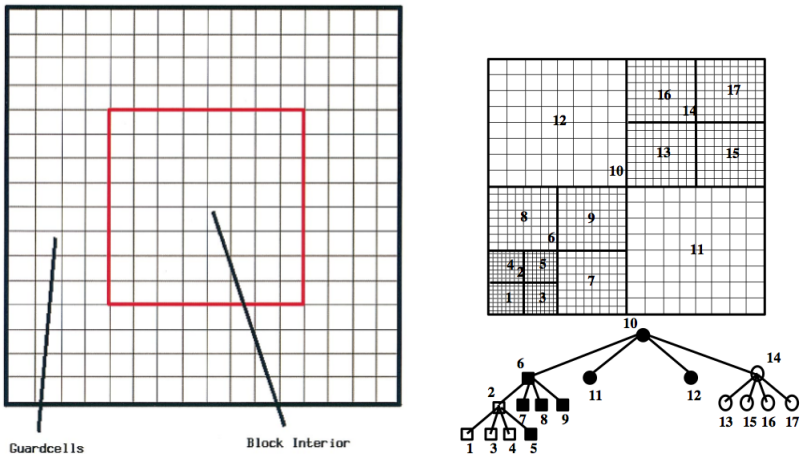

Figure 2.2: *Left panel*: A typical two dimensional block outlined in red. The cells exterior to the block are the ghost cells which are shared by neighboring blocks. *Right panel*: Outlines the procedure of a typical block being refined. The initial block is labeled 10 and is refined to produce four new sub-block, 6, 11, 12, and 14. Sub-blocks 6 and 14 are further refined. Below the right image shows the hierarchy of the block structure. Images reproduced from Fryxell et al. (2000).

would required a great deal of numerical resolution which results in a significant increase in computational time. Fortunately, FLASH is an adaptive mesh refinement (AMR) code, which is to say, that FLASH can add resolution (based on some user prescribed criteria) to areas needed and decreases areas not needed during the computation. FLASH conducts refinement in a hierarchical block-structured, that is when a block (a collection of cells) needs refinement it is sub-divided to a new set of sub-blocks (see Figure 2.2 and 2.3). These new sub-blocks are treated as standard blocks. Each subdivision has to adhere to three standard rules. First, each sub-block must be half as large in each spatial dimension. Second, the sub-block must be confined inside the refined block and must not overlap any other sub-block. Thus, each refinement level allows the block to be subdivided into 2^d sub-blocks, where d is the number of dimensions in the model. Lastly, neighboring blocks cannot differ more than one level of resolution. The derefinement is simply the reverse

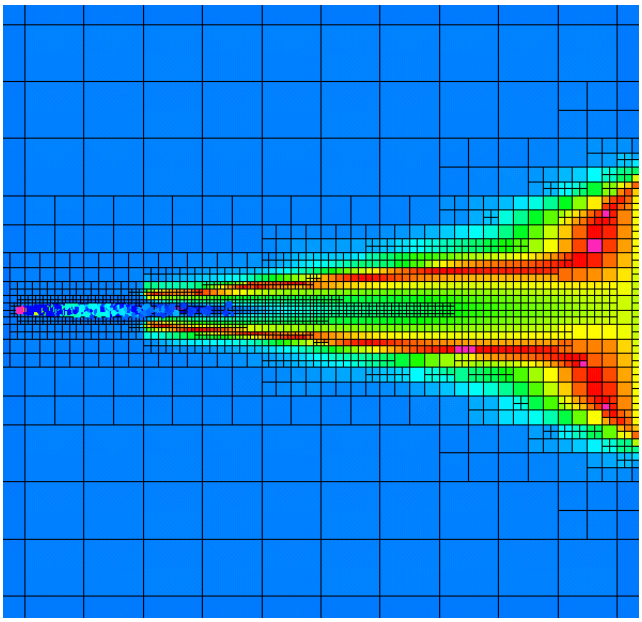

Figure 2.3: A simulation of a combustion diesel spray using adaptive mesh refinement–reproduced from Convergent Science, Inc.

process described.

The criteria used to determine when a block needs refinement or derefinment is based on work by Löhner (1987). The criteria amounts to computing second derivatives of the quantities chosen for refinement and normalizing by averaged gradients in the computational cell.

2.4 Numerical Tests

In the following sections we show how the FLASH code performs on two hydrodynamical problems, which have analytic solutions, the Sod shock tube and the Sedov explosion problem.

2.4.1 Sod

The sod problem (Sod 1978) is a one-dimensional flow discontinuity problem which we can check the code's ability to handle shocks and contact discontinuities. The problem consists of planar interface separating the initial fluid at rest. The region to the left of the interface has high density ρ_L and high pressure p_L, while the region to the right of the interface has low density ρ_R and low pressure p_R. Suddenly the interface is removed and a shock develops propagating from the high pressure region into the low pressure region.

The density and pressure from both regions are chosen so that all three types of flow discontinuities (shock, contact, and rarefaction) develop,

$$\rho_L = 1, \tag{2.6}$$

$$\rho_R = 0.125, \tag{2.7}$$

$$p_L = 1, \tag{2.8}$$

$$p_R = 0.1, \tag{2.9}$$

in dimensionless units. The ratio of specific heats γ is taken to be 1.4 on both regions. Figure 2.4 shows the solution obtained from FLASH with six levels of refinement compared with the analytic solution at time $t = 0.20$. Notice the three different wave types are present: a rarefaction between $x \approx 0.25$ and $x \approx 0.5$, a contact discontinuity at $x \approx 0.68$, and a shock at $x \approx 0.85$. The close agreement between FLASH and the analytic solution shows the ability of PPM to handle sharp features.

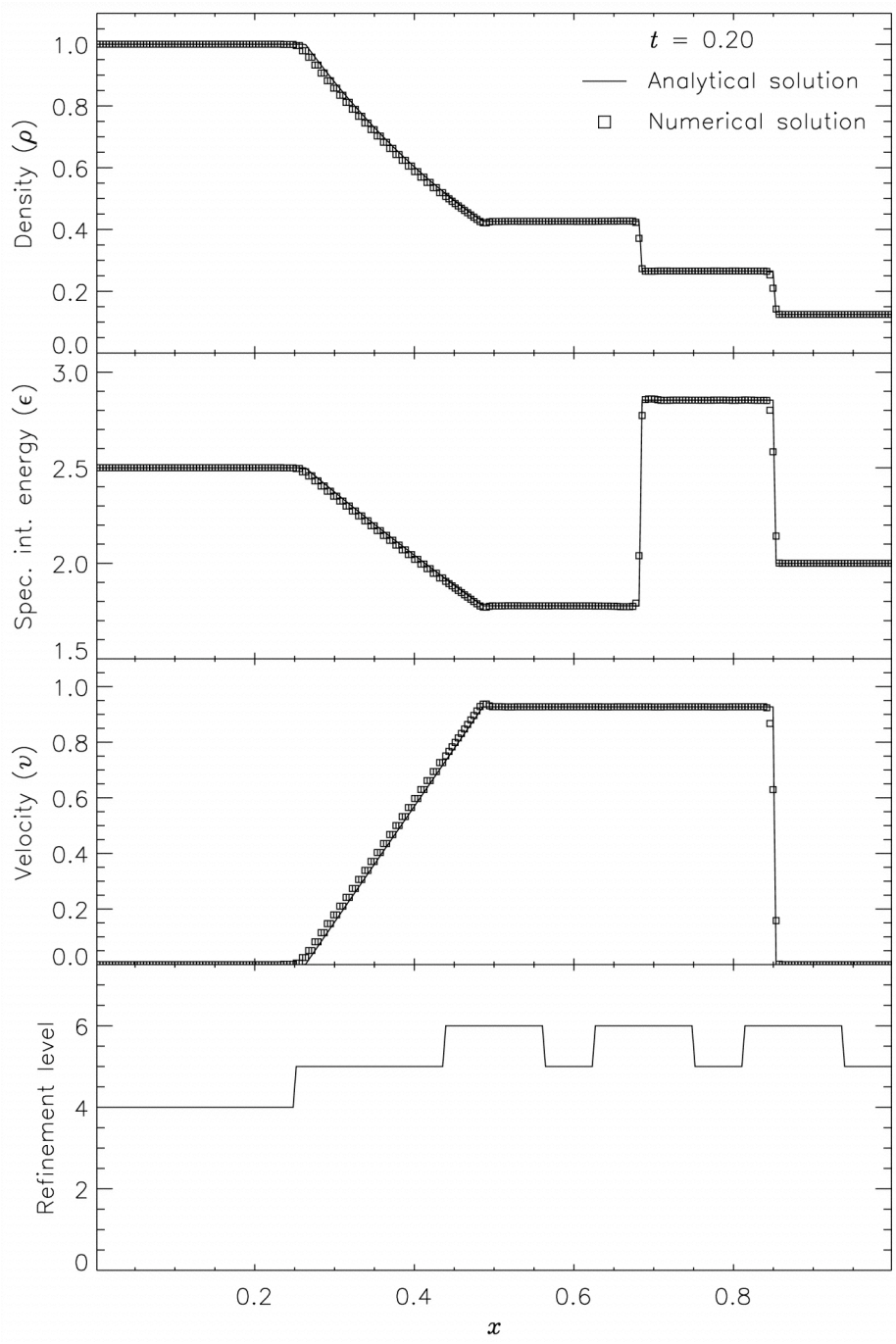

Figure 2.4: Comparison of numerical and analytical solutions to the Sod problem, with six levels of refinement at $t = 0.20$–reproduced from Fryxell et al. (2000).

2.4.2 Sedov

The Sedov explosion is a commonly used problem to verify a code's ability to deal with shocks. The Sedov problem originated from the need to model the effects of the atomic bomb during world war II. It was independently solved by Sedov (1946, 1959) and by Taylor (1950).

The Sedov problems allows a neat method for describing the size of the blast and the velocity of the shock front without solving the Euler equations, although a thorough treatment requires solving the Euler equations, e.g. Landau & Lifshitz (1959). The initial parameters for the problem are the energy E, which is instantaneously delivered to a point, and the surrounding uniform density ρ_0. Now from the given initial parameters there is no possible way to combine them to generate a time or length scale. Therefore, we suppose that there is a scale parameter λ which gives the size of the blast at time t after the explosion. Apart from being a monotonically increasing function of time, the evolution of λ may depend on E and ρ_0. Now there is only way of combing t, E, and ρ_0 to produce a time scale

$$\lambda = \left(\frac{Et^2}{\rho_0}\right)^{\frac{1}{5}}. \tag{2.10}$$

Letting $r(t)$ be the radius of any arbitrary shell inside the blast. We now introduce a dimensionless parameter

$$\xi \equiv \frac{r}{\lambda} = \left(\frac{\rho_0}{Et^2}\right)^{\frac{1}{5}}, \tag{2.11}$$

such that ξ does not change in time for a particular shell. Thus, each shell can be labeled by a paticluar ξ. Designating ξ_0 correspond to the shock front

$$r_s(t) = \xi_0 \left(\frac{Et^2}{\rho_0}\right)^{\frac{1}{5}}. \tag{2.12}$$

Thus, the velocity of the shock front is

$$v_s(t) = \frac{dr_s}{dt} = \frac{2}{5}\frac{r_s}{t} = \frac{2}{5}\xi_0 \left(\frac{E}{\rho_0 t^3}\right)^{\frac{1}{5}}. \tag{2.13}$$

So the size of the spherical blast increases as $t^{2/5}$ and the velocity of the front goes down as $t^{-3/5}$, or in other words the velocity falls off as $r_s^{-3/2}$.

Figure 2.5 shows the density, pressure, and velocity profiles of the cylindrical blast wave obtained from FLASH with 2, 4, 6, and 8 levels of refinement compared with the analytic solution at $t = 0.05$. The initial energy, density, and pressure where set to

$$E = 1, \tag{2.14}$$

$$\rho_0 = 1, \tag{2.15}$$

$$p_0 = 10^{-5}, \tag{2.16}$$

in dimensionless units. The ratio of specific heats γ is taken to be 1.4. At low resolutions, errors show up in the density and velocity profiles. However, we see the numerical solution converges to the analytic solution as the levels of refinement are increased. Lastly, Figure 2.6 shows the pressure field with eight levels of refinement at $t = 0.05$.

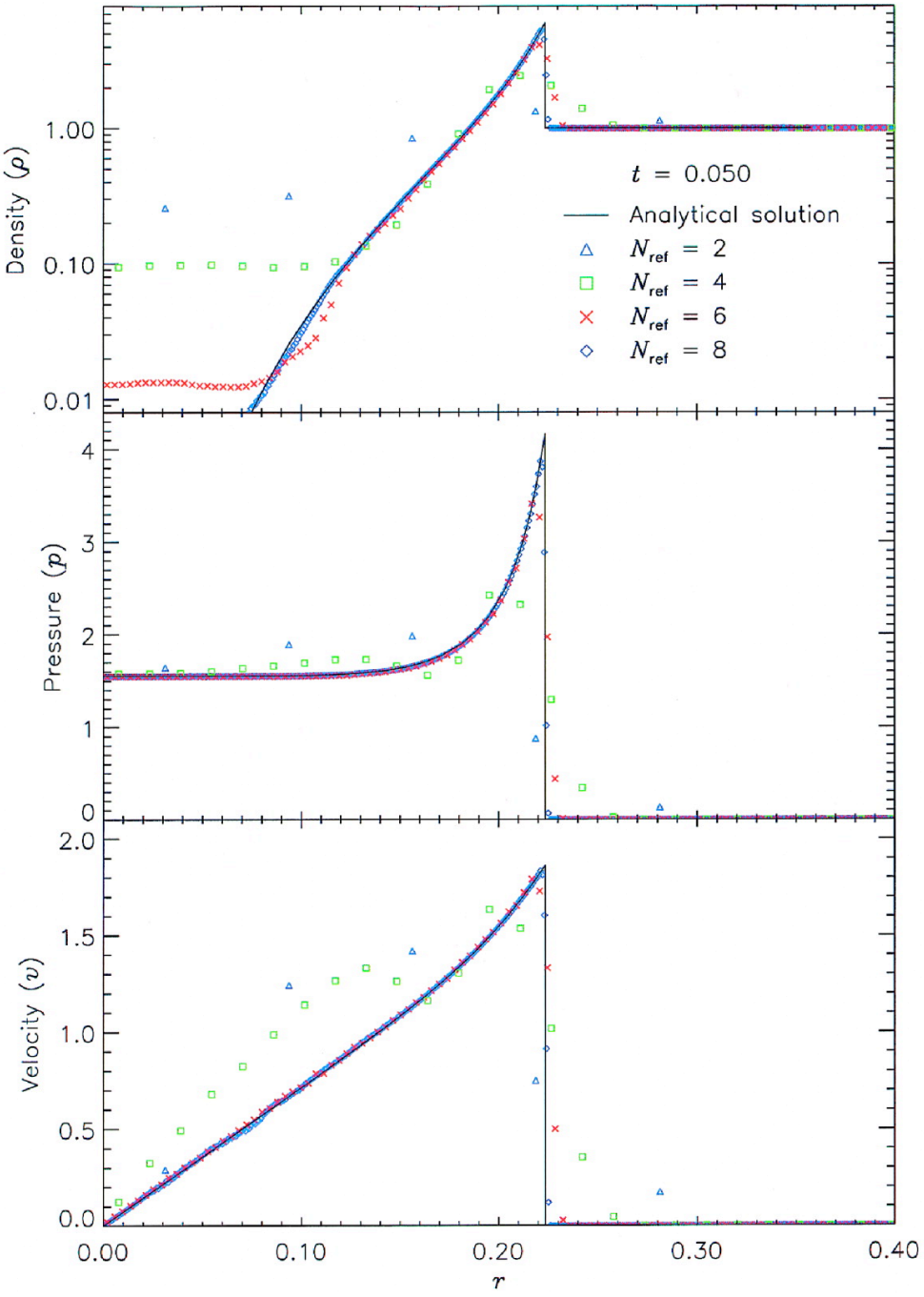

Figure 2.5: Comparison of numerical and analytical solutions to the Sedov problem in two dimension, with different level of refinement at $t = 0.05$–reproduced from Fryxell et al. (2000).

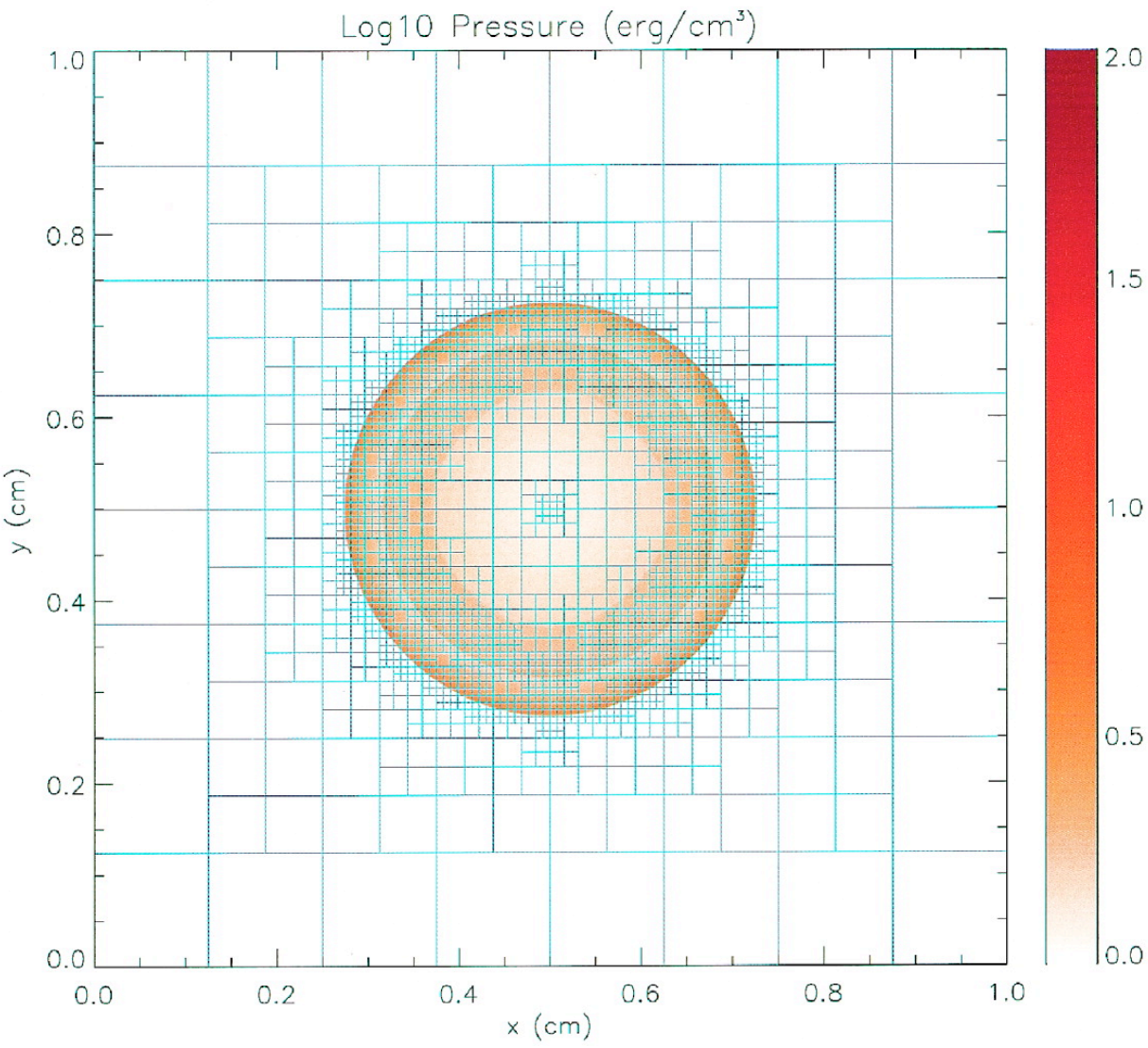

Figure 2.6: Pressure field in the two-dimensional Sedov explosion with eight levels of refinement at $t = 0.05$–reproduced from Fryxell et al. (2000).

2.5 Outline of Attack

With a method to solve the Euler equations, we are ready to calculate the feeding rates of MBHs due solely to the ingestion of winds from neighboring stars. Although we have the tools to attack the problem head on, it is still a formidable task. Instead, we first attack the problem without the MBH, that is, we calculate the possible flows due to the interaction from the stellar winds in a star cluster. This will gives us key insight when the potential well of the black hole is small. Also, it will give us a method to test our code since the problem has been done analytically by Cantó et al. (2000). Then we will add the interaction from the MBH and compare it with the work from Quataert (2004) which whom model the accretion of a SMBH in the Galactic Center. Finally, we use our formalism to model the globular cluster G1 with it's highly debated IMBH.

3

Retention of Stellar Winds in Core Potentials

3.1 Stellar Winds in Cluster of Stars

3.1.1 Analytic Solution

In this section we develop a spherical symmetrical model to describe the flow profile of multiple interacting stellar winds produced by a cluster of massive stars. This idealized model was developed by Cantó et al. (2000) and will provide the first test for our numerical formalism. The model consists of a cluster of $N_{\rm s}$ massive stars packed inside a cluster of radius $R_{\rm c}$. The cluster is embedded inside a gas cloud for which we take to be infinite in size with constant pressure $p(\infty)$ and density $\rho(\infty)$. Further, we assume each star ejects mass at a rate $\dot{M}_{\rm s}$ with a stellar wind velocity $v_{\rm w}$. The stellar mass loss rate per unit volume is given by

$$q(r) = \frac{3N(r)\dot{M}_{\rm s}}{4\pi r^3}, \tag{3.1}$$

where $N(r)$ is the number of stars enclosed by the radius r. For the present we will assume $q(r)$ is constant: $q = 3N_{\rm s}\dot{M}_{\rm s}/(4\pi R_{\rm c}^3)$ which amounts to setting the distribution of stars to $N(r) \propto r^3$. Hence, by defining $q(r)$ we also define the distribution of stars inside the cluster.

We are now ready to solve the equations of Hydrodynamics (see Appendix C for derivations). We are interested in steady adiabatic flows, this amounts to setting time derivatives to zero in the fluid equations and permits us to use the relation $p = K\rho^\gamma$, where K is a constant and γ is the ratio of specific heats. The fluid equations have the form

$$\nabla \cdot (\rho\,\vec{v}) = q \qquad \text{(Continuity Equation)} \tag{3.2}$$

$$\rho\,\vec{v} \cdot \nabla\,\vec{v} = -\nabla p - q\vec{v} \qquad \text{(Momentum Equation)} \tag{3.3}$$

$$\nabla \cdot \left[\left(\frac{1}{2}\rho v^2 + \rho\epsilon + p\right)\vec{v}\right] = \vec{v} \cdot (q\vec{v}). \qquad \text{(Energy Equation)} \tag{3.4}$$

We begin by solving the equations 3.2-3.4 interior to the cluster. Performing a volume integral at an arbitrary radius r inside the cluster, the continuity equation becomes

$$\iiint_V \nabla \cdot (\rho\vec{v})\,\mathrm{d}V = \oiint_S \rho\vec{v} \cdot \hat{n}\mathrm{d}S = \iiint_V q\,\mathrm{d}V \tag{3.5}$$

$$4\pi r^2 \rho v = \frac{4\pi r^3}{3} q, \tag{3.6}$$

where we have used the divergence theorem. Solving for ρ, we obtain the density in terms of the velocity and radius

$$\rho = \frac{qr}{3v}. \tag{3.7}$$

We turn our attention to the energy equation (3.6). Making use of the equation of state $p = (\gamma - 1)\,\rho\epsilon$, we have the following

$$\nabla \cdot \left[\left(\frac{1}{2}\rho v^2 + \rho \left(\frac{1}{\gamma - 1}\frac{p}{\rho} \right) + p \right) \vec{v} \right] = \vec{v} \cdot (q\vec{v}) \tag{3.8}$$

$$\nabla \cdot \left[\left(\frac{1}{2}\rho v^2 + \frac{\gamma}{\gamma - 1}p \right) \vec{v} \right] = \vec{v} \cdot (q\vec{v}). \tag{3.9}$$

Performing the same volume integral as we did for the continuity equation

$$\iiint_V \nabla \cdot \left[\left(\frac{1}{2}\rho v^2 + \frac{\gamma}{\gamma - 1}p \right) \vec{v} \right] \mathrm{d}V = \iiint_V \vec{v} \cdot (q\vec{v}) \mathrm{d}V \tag{3.10}$$

$$\oiint_S \left[\left(\frac{1}{2}\rho v^2 + \frac{\gamma}{\gamma - 1}p \right) \vec{v} \right] \cdot \hat{n} \mathrm{d}S = \iiint_V \vec{v} \cdot (q\vec{v}) \mathrm{d}V. \tag{3.11}$$

The term on the right hand side, as explained in appendix D, is the total rate injection of energy. This value can be calculated as follows. In a small amount of time Δt an amount of mass $q\Delta t \Delta V$ is ejected. It carries kinetic energy $1/2(q\Delta t \Delta V)v_{\mathrm{w}}^2$. Hence, the rate of energy injection per volume is $qv_{\mathrm{w}}^2/2$. So then the total energy injection rate is

$$\iiint_V \vec{v} \cdot (q\vec{v}) \mathrm{d}V = \frac{1}{2} q v_{\mathrm{w}}^2 \frac{4\pi r^3}{3}. \tag{3.12}$$

So now the energy equation has the following form

$$\left(\frac{1}{2}\rho v^2 + \frac{\gamma}{\gamma - 1}p \right) 4\pi r^2 \rho v = \frac{1}{2} q v_{\mathrm{w}}^2 \frac{4\pi r^3}{3}. \tag{3.13}$$

Dividing equation 3.8 with 3.18 gives

$$\frac{1}{2}v^2 + \frac{\gamma}{\gamma - 1}\frac{p}{\rho} = \frac{1}{2}v_{\mathrm{w}}^2 \tag{3.14}$$

Turning our attention to the momentum equation

$$\rho v \frac{dv}{dr} = -\frac{dp}{dr} - \frac{3N_{\mathrm{s}}\dot{M}_{\mathrm{s}}v}{4\pi R_{\mathrm{c}}^3}, \tag{3.15}$$

and the adiabatic sound speed

$$c^2 = \gamma \frac{p}{\rho}, \tag{3.16}$$

we can rewrite equation 3.14 and 3.15 as

$$c^2 = \frac{\gamma - 1}{2}\left(v_{\rm w}^2 - v^2\right), \tag{3.17}$$

$$\rho v \frac{dv}{dr} = -\frac{1}{\gamma}\frac{d\left(\rho c^2\right)}{dr} - \frac{3N_{\rm s}\dot{M}_{\rm s}v}{4\pi R_{\rm c}^3}. \tag{3.18}$$

Now substituting equations 3.7 and 3.17 into 3.18 and introducing new dimensionless variables $V \equiv v/v_{\rm w}$ and $R \equiv r/R_{\rm c}$ equation 3.18 becomes

$$\left[\frac{(\gamma-1) - (\gamma+1)V^2}{(\gamma-1) - (5\gamma+1)V^2}\right]\frac{dV^2}{V^2} = 2\frac{dR}{R}. \tag{3.19}$$

Integration of equation 3.19 leads to the the velocity profile inside the cluster

$$V\left[1 + \frac{5\gamma+1}{\gamma-1}V^2\right]^{-(3\gamma+1)/(5\gamma+1)} = \alpha R, \tag{3.20}$$

where α is a constant of integration. Instantly, we see that $V = 0$ for $R = 0$ and because equation 3.20 is a monotonically increasing function, the velocity inside the cluster increases from zero to some max value at $R_{\rm c}$.

Outside the cluster $q = 0$ and it follows from the continuity equation

$$\frac{4\pi}{3}N_{\rm s}\dot{M}_{\rm s} = 4\pi r^2 \rho v. \tag{3.21}$$

Substituting equations 3.17 and 3.21 into equation 3.18 and integrating gives

$$V\left(1 - V^2\right)^{1/(\gamma-1)} = \frac{\beta}{R^2}, \tag{3.22}$$

where β is a constant of integration.

Equation 3.22 implies as $R \to \infty$, $V \to 0$ (asymptotically subsonic flow) or $V \to 1$ (asymptotically supersonic flow). We now have a clear understanding, the interactions of the stellar winds produce a flow which is zero at the center of the cluster and for which it grows to max value at R_c. From that point onward, the flow can adopt a subsonic flow

or a supersonic flow depending on the boundary conditions far away from the cluster. We can calculate the corresponding density, sound speed, and pressure at $R \to \infty$ for both situations.

For the subsonic case, multiplying equation 3.22 with 3.21 and taking the limit as $R \to \infty$ we have

$$\rho_{\rm sub}\left(\infty\right) = \frac{N_{\rm s}\dot{M}_{\rm s}}{4\pi\beta R_{\rm c}^2 v_{\rm w}}. \tag{3.23}$$

Using equation 3.17 and 3.16 in the limit gives

$$c_{\rm sub}^2(\infty) = \frac{\gamma-1}{2}v_{\rm w}^2, \tag{3.24}$$

$$p_{\rm sub}(\infty) = \frac{\gamma-1}{2\gamma}\frac{N_{\rm s}\dot{M}_{\rm s}v_{\rm w}}{4\pi\beta R_{\rm c}^2}. \tag{3.25}$$

For the supersonic case

$$\rho_{\rm sup}(\infty) = c_{\rm sup}^2(\infty) = p_{\rm sup}(\infty) = 0. \tag{3.26}$$

For the subsonic case, the limiting values should coincide with the values of the gas cloud (i.e $\rho(\infty)$ and $p(\infty)$). Therefore, β is determined by equation 3.25

$$\beta = \frac{\gamma-1}{2\gamma}\frac{N_{\rm s}\dot{M}_{\rm s}v_{\rm w}}{4\pi p(\infty)R_{\rm c}^2}. \tag{3.27}$$

The question then arises: what is the minimum pressure needed for the outflow to be subsonic? Certainly if the pressure of the gas cloud $p(\infty)$ is less then this value then the flow can not be held back and then the flow becomes supersonic. From equation 3.22 at $R = 1$ (i.e, at $r = R_{\rm c}$) we have

$$V(1)\left(1 - V(1)^2\right)^{1/(\gamma-1)} = \beta, \tag{3.28}$$

for which β reaches its maximum vale of

$$\left(\frac{\gamma-1}{\gamma+1}\right)^{1/2}\left(\frac{2}{\gamma+1}\right)^{\gamma/(\gamma-1)} \tag{3.29}$$

for

$$V(1) = \left(\frac{\gamma - 1}{\gamma + 1}\right)^{1/2}. \tag{3.30}$$

Therefore, if

$$P < \frac{1}{\gamma}\left(\frac{\gamma - 1}{\gamma + 1}\right)^{1/2}\left(\frac{\gamma + 1}{2}\right)^{\gamma/(\gamma-1)}\frac{N_{\rm s}\dot{M}_{\rm s}v_{\rm w}}{4\pi R_{\rm c}^2} \tag{3.31}$$

then the subsonic solution is not possible and the flow becomes supersonic with α and β obtaining their limiting values

$$\alpha = \left(\frac{\gamma - 1}{\gamma + 1}\right)^{1/2}\left(\frac{\gamma + 1}{6\gamma + 2}\right)^{(3\gamma+1)/(5\gamma+1)} \tag{3.32}$$

$$\beta = \left(\frac{\gamma - 1}{\gamma + 1}\right)^{1/2}\left(\frac{2}{\gamma + 1}\right)^{\gamma/(\gamma-1)}. \tag{3.33}$$

Figures 3.1 and 3.2 show the density and velocity profiles for the values $N_{\rm s} = 30$, $\dot{M}_{\rm s} = 10^{-5}\,M_{\odot}\,{\rm year}^{-1}$, $v_{\rm w} = 10^{8}\,{\rm cm\,s}^{-1}$, $\gamma = 5/3$ and $R_{\rm c} = 6.5 \times 10^{17}\,{\rm cm}$. Interior to the cluster, the gas accumulated creates a high density region whose density decreases slightly as one moves away from the center. Near $R_{\rm c}$ is the largest density variation which produces a large pressure support that drives out the gas. The high pressure gradient creates the highest increase in velocity. Away from the cluster the pressure support fades away as the gas slowly accelerates before reaching $v_{\rm w}$.

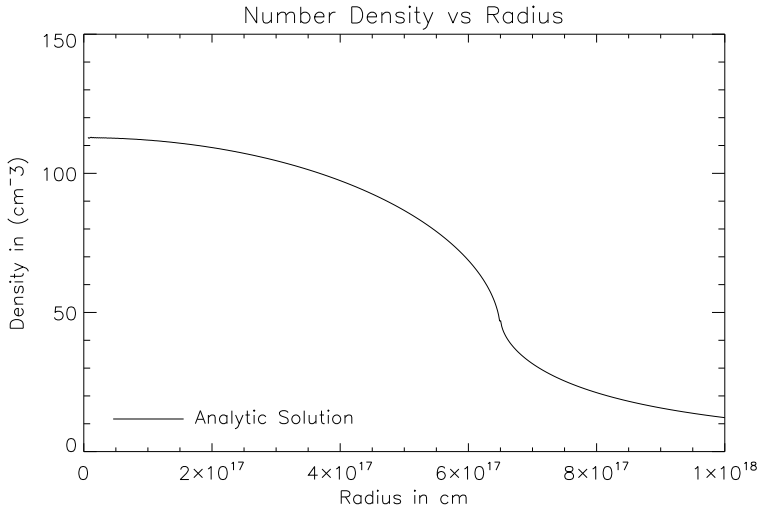

Figure 3.1: *Number Density vs. Radius* from the stellar winds of 30 stars distributed uniformly in a sphere of radius $R_{\rm c} = 6.5 \times 10^{17}$ cm, with all stars having the same mass loss rate $\dot{M}_{\rm s} = 10^{-5}\, M_{\odot}\,{\rm year}^{-1}$, and wind velocity $v_{\rm w} = 10^{8}\,{\rm cm/s}$.

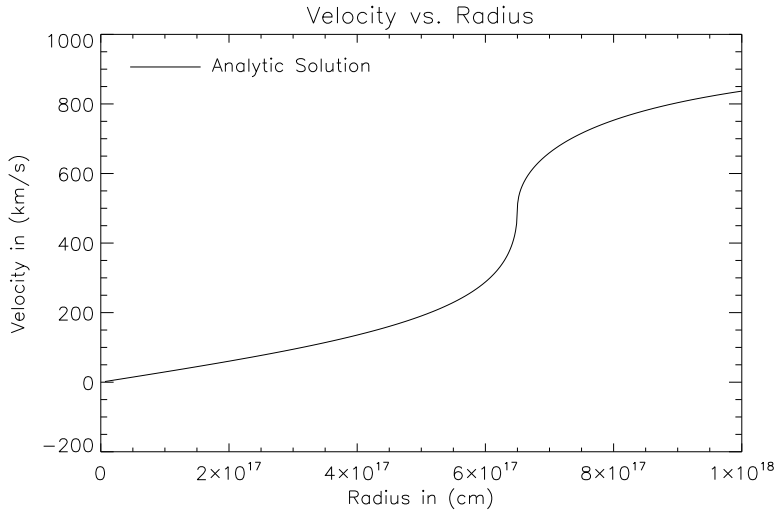

Figure 3.2: *Velocity vs. Radius* for the values stated in this section. The velocity at the origin is zero and increases monotonically until it reaches $R_{\rm c}$. The large increase in velocity at $R_{\rm c}$ is due to the density drop which creates a large pressure which drives out the gas. Outside the cluster the gas approaches $v_{\rm w}$ monotonically.

3.1.2 Numerical Solution by FLASH

To implement the stellar mass loss rate per unit volume $q(r)$ and the rate of energy injection per unit mass $v_{\rm w}^2/2$ in FLASH, we update the computed density and energy at each time step in every cell. Thus, inside the cluster the density at every cell is updated to $\rho_{\rm new} = \rho_{\rm old} + qdt$. To conserve momentum the velocity at each cell is corrected to $v_{\rm new} = \rho_{\rm old}\, v_{\rm old}/\rho_{\rm new}$. Now the specific energy (energy per unit mass) is affected by two contributions. First due to the increase of mass and second by the addition of thermal energy from the stellar winds. Therefore the new energy per unit volume is $\rho_{\rm new}\, E_{\rm new}$ (to account for the mass increase) which is equal to $\rho_{\rm old}\, E_{\rm old} + q\, dt\, v_{\rm w}^2/2$ (to account for the energy increase). Remembering that energy is comprised of the internal and kinetic contribution, $E = \epsilon + v^2/2$, we summarize the updated quantities at each time step and in every cell:

$$\rho_{\rm new} = \rho_{\rm old} + q\, dt \tag{3.34}$$

$$v_{\rm new} = \rho_{\rm old}\, v_{\rm old}/\rho_{\rm new} \tag{3.35}$$

$$\epsilon_{\rm new} = \frac{\rho_{\rm old}}{\rho_{\rm new}} \left(\epsilon_{\rm old} + v_{\rm old}^2\right) - \frac{1}{2} v_{\rm new}^2 + \frac{1}{2}\, q\, dt\, v_{\rm w}^2. \tag{3.36}$$

Figures 3.3 and 3.4 show the density and velocity profiles compared with the analytic and FLASH solution. For the density we see that the solution obtained from FLASH closely matches the analytic from the origin to $R_{\rm c}$. Outside $R_{\rm c}$ the density differs only slightly and then converges back to the solution. For the velocity profile the FLASH solution is in good agreement with the analytical formalism.

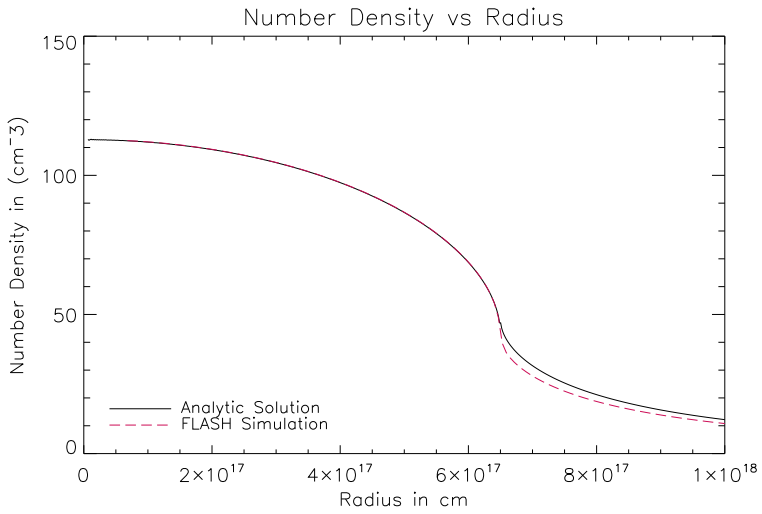

Figure 3.3: Comparison of the analytic solution of *Density vs. Radius* with our numerical formalism. Interior to the cluster the numerical solution is in exact agreement with the analytical solution. At R_c there are small deviations which tend to zero at larger distances from the cluster.

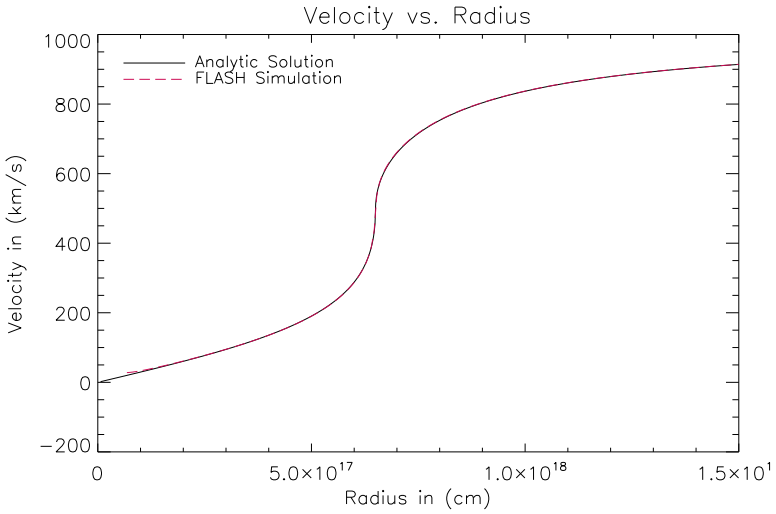

Figure 3.4: Comparison of the analytic solution of *Velocity vs. Radius* with our numerical formalism. The numerical solution is in agreement with the analytical for all radii in the computation domain.

3.2 Stellar Winds in Clusters with Realistic Potentials

In the previous section we have ignored the effects of gravity from the stellar members. This can be justified by comparing the sound speed of the shocked gas to the escape velocity from the cluster. The sound speed is $\sqrt{\gamma p/\rho}$ and the pressure should be on the order of $\rho v_{\rm w}^2$, where ρ is density of the winds. So then the sound speed

$$c_{\rm s} = \sqrt{\frac{\gamma p}{\rho}} \approx \sqrt{\frac{\gamma \rho v_{\rm w}^2}{\rho}} \approx v_{\rm w}. \tag{3.37}$$

while

$$v_{\rm es} = \sqrt{\frac{2GM}{r}} \approx \sqrt{\frac{2GN_{\rm s}M_{\rm s}}{R_{\rm c}}}, \tag{3.38}$$

where G is the gravitational constant, and $N_{\rm s}$ is the number of stars of mass $M_{\rm s}$ in the cluster of radius $R_{\rm c}$. Comparing the speeds from the values used in the previous section and with $M_{\rm s} = 10 M_{\odot}$ we have

$$v_{\rm es} \approx 4 \, \frac{\rm km}{\rm s} \ll {\rm c_s} \approx 10^3 \, \frac{\rm km}{\rm s}. \tag{3.39}$$

Clearly the gravitational force from the stellar members is negligible but looking back at our analysis we observe that if the stellar winds are considerably low and/or the stellar cluster is compact, then the escape velocity and the sound speed can be comparable.

In our current formalism we can easily incorporate the effects of the gravitational force due to the stellar members. At each time step and at every cell the velocity changes due to the gravitational force and the addition of mass. From section 3.1.2 the velocity was updated to $v \rightarrow \rho_{\rm old} v_{\rm old}/\rho_{\rm new}$. Now accounting for the gravitational force the new velocity is

$$v_{\rm new} = \rho_{\rm old} v_{\rm old}/\rho_{\rm new} - \frac{GM(r)}{r^2} dt, \tag{3.40}$$

where $M(r)$ is the mass of the stellar members enclosed at a distance r. Further, we can extend our formalism to include the gravity of a BH by letting $M(r) \rightarrow M(r) + M_{\rm BH}$, where $M_{\rm BH}$ is the mass of the BH.

Figures 3.6 and 3.5 show the velocity and density profiles including the gravity of the stellar members. The values taken where the same as the previous section except $N_{\rm s} = 1000$ and $v_{\rm w} = 50\,{\rm km\,s^{-1}}$. The new escape speed is $v_{\rm es} \approx 14\,{\rm km\,s^{-1}}$. The addition of the gravitational force increases the density inside the cluster due to the retention of the gas. Although there is a larger pressure support it now has to compete with gravity, which results in a net decrease in velocity outside the cluster.

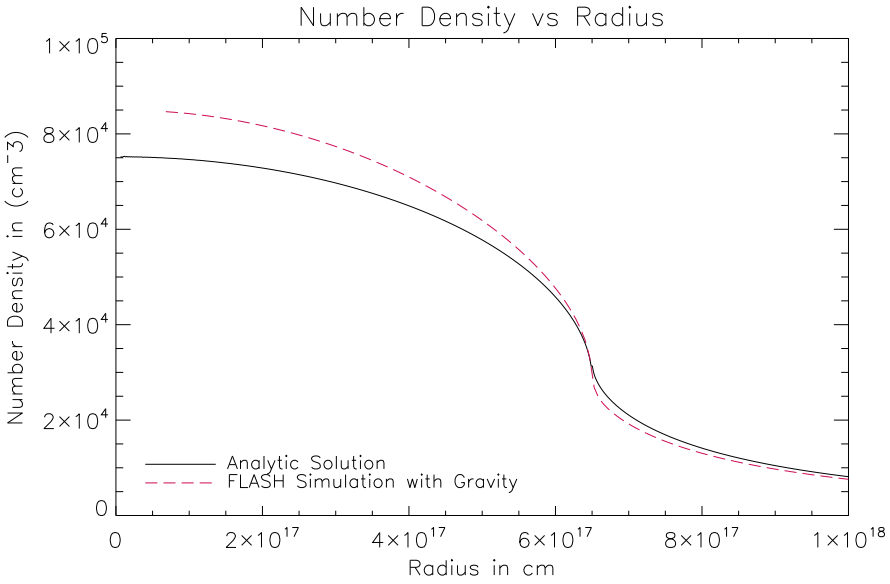

Figure 3.5: *Number Density vs. Radius* from the stellar winds of 1000 stars distributed uniformly in a sphere of radius $R_{\rm c} = 6.5 \times 10^{17}\,{\rm cm}$, with all the stars having the same mass loss rate $\dot{M}_{\rm s} = 10^{-5}\,M_{\odot}\,{\rm year}^{-1}$, mass $M_{\rm s} = 10 M_{\odot}$, and wind velocity $v_{\rm w} = 50\,{\rm km\,s^{-1}}$. The gravity from the stellar members retains a fraction of the outflow gas, resulting to an increase of density inside the cluster.

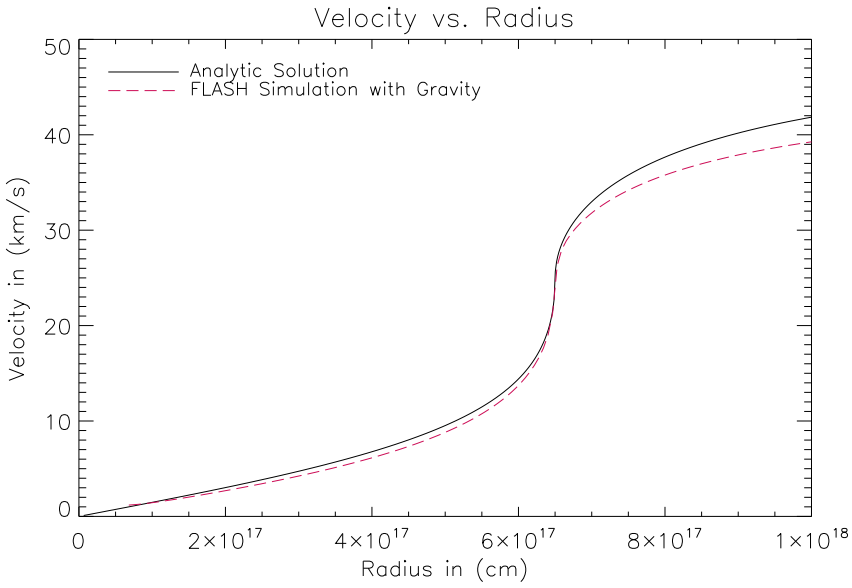

Figure 3.6: Comparison of the analytic solution of *Velocity vs. Radius* with the numerical obtained by FLASH. The addition of the gravitational force from the stellar members results in decreasing the outflow speed.

4

Feeding Black Holes with Stellar Winds

4.0.1 Steady, Spherically Symmetric Accretion

Before we embark modeling the Galactic Center and nuclei of the globular cluster G1, it will be useful to gain a thorough understanding of how a massive body, a BH in our case, embedded in a medium which accretes from its local surrounding. This analysis was originally done by Bondi (1952) and will help us guide our physical intuition of the problem at hand.

Our treatment begins by considering a BH of mass M embedded in a gas of ambient density $\rho(\infty)$ and sound speed $c_s(\infty)$. Due to the rotational symmetry of the problem we take the coordinates to be spherical which in turn leads to only the analysis of the radial coordinate r. From the continuity equation in steady state it follows

$$\frac{1}{r^2}\frac{d}{dr}\left(r^2\rho v\right) = 0, \tag{4.1}$$

which implies the quantity $r^2\rho v$ is constant. The quantity $4\pi r^2\rho v$ represents the rate which gas flows through a spherical shell, centered at the BH, of area $4\pi r^2$. According to equation 4.1 this rate is constant

$$\dot{M} \equiv 4\pi r^2 \rho v, \tag{4.2}$$

which also happens to be the accretion rate onto the BH.

Utilizing the momentum equation and noting that the only external force is due to gravity, $f_r = GM\rho/r^2$, we have

$$\rho v \frac{dv}{dr} = -\frac{dp}{dr} - \frac{GM\rho}{r^2}. \tag{4.3}$$

For the energy equation, it is often possible to replace it by the polytropic equation

$$p = K\rho^\gamma, \tag{4.4}$$

where K is a constant and γ is the ratio of specific heats. From the polytropic equation the quantity dp/dr can be manipulated to

$$\frac{dp}{dr} = \frac{dp}{d\rho}\frac{d\rho}{dr} = c_s^2 \frac{d\rho}{dr}, \tag{4.5}$$

where we have used $c_s^2 = dp/d\rho$ (see Appendix D). From the continuity equation we have the following relation

$$\frac{d}{dr}\left(r^2\rho v\right) = 0 \tag{4.6}$$

$$r^2 v \frac{\rho}{dr} + \rho \frac{r^2 v}{dr} = 0 \tag{4.7}$$

or

$$\frac{1}{\rho}\frac{d\rho}{dr} = -\frac{1}{r^2 v}\frac{d\left(r^2 v\right)}{dr}. \tag{4.8}$$

Inserting equation 4.5 and 4.8 into the momentum equation and rearranging terms we get

$$\frac{1}{2}\left(1-\frac{c_s^2}{v^2}\right)\frac{dv^2}{dr} = -\frac{GM}{r^2}\left(1-\frac{2c_s^2 r}{GM}\right). \tag{4.9}$$

Now from equation (4.9) we can extract the behaviour of the flow. Intuitively, we expect that if we are infinitely far away from the BH the gas is essentially at rest due the r^{-2} dependence of gravity. As we approach from infinity to the BH the gravitational force increases and therefore the matter begins to pick up an inward velocity which increases as we approach the BH. With this in mind lets see what we can extract from equation 4.9. At large radii the right hand side of equation (4.9) is positive since $c_s^2 \to c_s(\infty)$ as $r \to \infty$. We expect the velocity to increase as it approaches the BH, this can be stated mathematically as $dv^2/dr < 0$. Thus, for the left hand side to be positive $c_s^2 > v^2$, that is, the flow is subsonic. For decreasing radii, the term in the parenthesis on the left hand side becomes less negative until it ultimately becomes zero at the radius

$$r_s = \frac{GM}{2c_s(r_s)^2}. \tag{4.10}$$

After this radial position, the term in the parenthesis on the right hand side becomes positive, hence the left hand side must now be negative. On the left hand side the term dv^2/dr can only become more negative since v is steadily increasing. As a result, $v^2 > c_s^2$, the flow becomes supersonic. Without solving equation (4.9) we have a physical description of the flow. The fluid is at rest at infinity and as we approach closer to the BH the velocity increase steadily. When we reach the distance $r_s = GM/2c_s(r_s)^2$ the fluid makes a transition from subsonic to supersonic and keeps increasing as it makes its final destination to the BH.

It turns out that the solution we have just described is only one out of six classes of possible solutions. The other classes are supersonic solutions for all radii, stellar winds,

stellar breezes, and lastly two classes which are deemed non-physical because they are double valued at each radial position.

Armed with our new insight we can proceed to integrate equation (4.3)

$$\int v\,\mathrm{d}v + \int \frac{\mathrm{d}p}{\rho} + \int \frac{GM}{r^2}\mathrm{d}r = 0 \tag{4.11}$$

$$\frac{1}{2}\int \mathrm{d}v^2 + \int \frac{\mathrm{d}p}{\rho} + \int \frac{GM}{r^2}\mathrm{d}r = 0 \tag{4.12}$$

$$\frac{1}{2}v^2 + \int \frac{\mathrm{d}p}{\rho} - \frac{GM}{r} = \text{constant}. \tag{4.13}$$

From the polytropic relation, $p = K\rho^{\gamma}$, we have $\mathrm{d}p = K\gamma\rho^{\gamma-1}\mathrm{d}\rho$. Then

$$\int \frac{\mathrm{d}p}{\rho} = \int K\gamma\rho^{\gamma-2}\mathrm{d}\rho = \frac{K\gamma\rho^{\gamma-1}}{\gamma-1} = \frac{\gamma p}{\rho\,(\gamma-1)} = \frac{c_s^2}{\gamma-1}, \tag{4.14}$$

where we have used $c_s^2 = dp/d\rho = \gamma p/\rho$. Therefore, equation (4.13) is now written as

$$\frac{1}{2}v^2 + \frac{c_s^2}{\gamma-1} - \frac{GM}{r} = \text{constant}. \tag{4.15}$$

We can find the constant of integration by imposing the condition $v \to 0$ as $r \to \infty$

$$0 + \frac{c_s^2(\infty)}{\gamma-1} - 0 = \text{constant}. \tag{4.16}$$

Now at the sonic point $v^2 = c_s^2$ and $r_s = GM/2c_s^2(r_s)$ so from equation (4.15) we have

$$\frac{1}{2}c_s^2(r_s) + \frac{c_s^2(r_s)}{\gamma-1} - GM\frac{2c_s^2(r_s)}{GM} = \frac{c_s^2(\infty)}{\gamma-1} \tag{4.17}$$

or

$$c_s^2(r_s) = c_s^2(\infty)\left(\frac{2}{5-3\gamma}\right)^{1/2}. \tag{4.18}$$

We have just found the sound speed at the sonic transition which depends solely on the ambient values of the gas. Likewise, the sonic point and the density at the sonic point can

be written in terms of the ambient variables

$$r_s = \frac{GM}{2c_s^2(\infty)}\left(\frac{5-3\gamma}{2}\right) \tag{4.19}$$

$$\rho(r_s) = \rho(\infty)\left(\frac{2}{5-3\gamma}\right)^{1/(\gamma-1)}. \tag{4.20}$$

Finally, we can obtain $\dot{M}$

$$\dot{M} = 4\pi r^2 \rho v = 4\pi r_s^2 \rho_s v_s \tag{4.21}$$

or

$$\dot{M} = \pi G^2 M^2 \frac{\rho(\infty)}{c_s^3(\infty)}\left[\frac{2}{5-3\gamma}\right]^{(5-3\gamma)/2(\gamma-1)}. \tag{4.22}$$

Again, the accretion rate is determined solely on the ambient values of the gas.

Additionally, we introduce the accretion rate radius $r_{\rm acc}$, which denotes the BHs hydrodynamical sphere of influence. The gas becomes bound to the BH when $c_s \to c_s(\infty)$, from equation (4.15)

$$\frac{1}{2}v^2 - \frac{GM}{r} \approx 0. \tag{4.23}$$

At large radii $v \to c_s(\infty)$ so then the accretion radius is

$$\frac{1}{2}c_s^2(\infty) - \frac{GM}{r_{\rm acc}} \approx 0 \tag{4.24}$$

or

$$r_{\rm acc} \approx \frac{2GM}{c_s^2(\infty)}. \tag{4.25}$$

Stated in a different way, at a distance r the ratio of the thermal energy to the gravitational binding energy for a gas particle of mass m is

$$\frac{\text{Thermal Energy}}{\text{Binding Energy}} \sim \frac{mc_s^2(r)}{2}\frac{r}{GMm} \sim \frac{r}{r_{\rm acc}} \text{ for } r \gtrsim r_{\rm acc}. \tag{4.26}$$

Hence, for $r \gg r_{\rm acc}$ the gravitational pull from the BH becomes negligible.

Lastly, in cases where $v \gg c_s(\infty)$ at distances far from the BH, the accretion radius is determined not by the ambient sound speed of the gas, but rather by the velocity of the flow relative to the BH. In this case, $\dot{M}$ transforms to

$$\dot{M} \sim \pi G^2 M^2 \frac{\rho(\infty)}{v^3(\infty)}. \tag{4.27}$$

4.0.2 Galactic Center

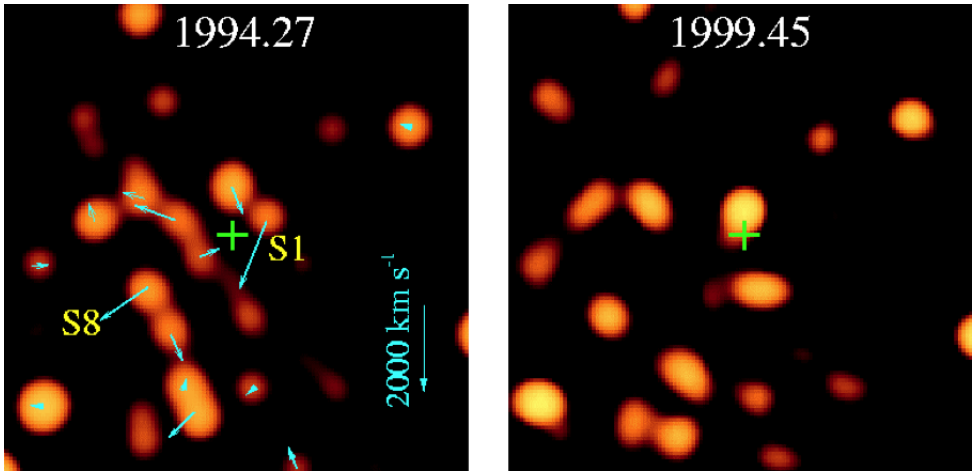

Figure 4.1: Images of Sagittarius A* (green cross) and the surrounding star cluster. The green arrows on the left image point to the new positions of the stars, shown on the right image, during the elapse time of 5.18yr. Through the measurements of the motions of the stars, the presence of a SMBH has been inferred–reproduced from Kormendy et al. (2001)

A compact radio source has been long known to be lurking at the Galactic Center with a radio luminosity on the order of $10^{34}\mathrm{erg\,s^{-1}}$ (Kormendy et al. 2001), commonly referred to as Sagittarius A*. A group lead by Reinhard Genzel and a group lead by Andrea Ghez independently measured the proper motions of stars at radii $\simeq 0.2\,\mathrm{pc}$ from Sagittarius A* (see Figure 4.1). From the proper motions they were able to infer the enclosed mass $M(r)$ (see Figure 4.2). At a distance of a couple of parsecs away from Sagittarius A*, the distribution of the stars dominate but as $r \to 0$, $M(r)$ becomes a constant value, signaling

the presence of a massive compact body. Measurements of stellar dynamics have confidently established that the nucleus of our galaxy harbors a SMBH with mass $M = 2.61 \times 10^6 M_\odot$ (Genzel et al. 1997).

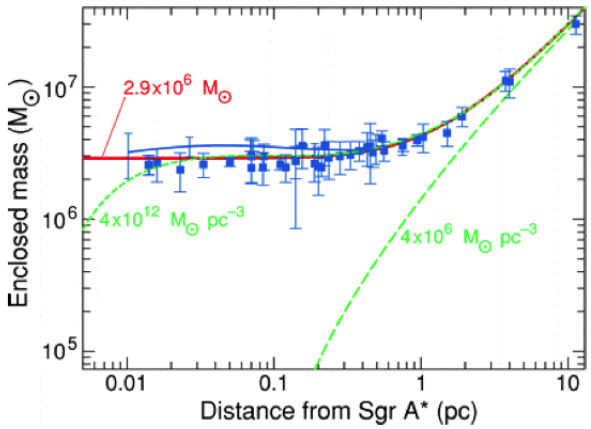

Figure 4.2: Enclosed mass inferred by the proper motions of stars surrounding Sagittarius A*. As the distance from Sagittarius decreases the enclosed mass becomes constant, revealing the presence of a SMBH–reproduced from Kormendy et al. (2001).

Quataert (2004) modelled the Galactic Center, incorporating both accretion onto the SMBH and the wind from the central star cluster, to describe the observed X-ray emission of the hot gas. Comparing our numerical formalism with Quataert's model will serve as a good test.

Before we begin modeling the Galactic Center with our formalism we can roughly predict the expected behavior of the gas. From our analysis in §3 we expect that far from the cluster the flow velocity should approach v_w. Inside the cluster the gas should develop an inflow onto the BH with an accretion rate roughly predicted by the Bondi Formula, $\dot{M}_\mathrm{BH} \sim \pi G^2 M^2 \rho(\infty)/v^3(\infty)$. The SMBH in the Galactic Center is surrounded by a medium with an average particle density $n \sim 10^3\,\mathrm{cm}^{-3}$ and a flow velocity $v(\infty) \sim 1000\,\mathrm{km\,s}^{-1}$ (Melia 2009). Therefore, the accretion rate onto the SMBH should be on the order of

$\dot{M} \sim 10^{-5} M_\odot\,\mathrm{yr}^{-1}$. Armed with a description of the flow we are ready to model the Galactic Center.

At the central parsec of the Galactic Center, gas is supplied by winds which originate from the interaction of several dozen massive stars (e.g., Krabbe et al. 1991; Najarro et al. 1997). These stars include blue supergiants with mass loss rates $\sim 10^{-4} M_\odot\,\mathrm{yr}^{-1}$ and wind speeds of $v_\mathrm{w} \approx 600 - 1000\,\mathrm{km\,s}^{-1}$ (e.g., Najarro et al. 1997). Following Quataert's model we take the total stellar mass loss rate to be $N_\mathrm{s}\dot{M}_\mathrm{s} = 10^{-3} M_\odot\,\mathrm{yr}^{-1}$ and $v_\mathrm{w} = 1000\,\mathrm{km\,s}^{-1}$. The mass loss spatial distribution is taken to be $q(r) \propto r^{-\eta}$ for $r \in [2'', 10'']$ and $q(r) = 0$ otherwise, where $\eta \in \{0, 2, 3\}$. The result of different values of η correspond to different mass loss distributions. For example, a value of $\eta = 0$ correspond to mass injection concentrated at large radii while $\eta = 3$ corresponds to equal mass injection for all radii interior to the cluster.

Figures 4.3 and 4.4 compare our formalism with Quataert's model of the Galactic Center. After many sound crossing times our solution settles into a steady state. The flow far away from the cluster, as expected, is driven out by a wind while interior to the cluster the the gas is captured and accreted onto the BH. The accretion rates for the three solutions from our model vary from $\sim 2 - 6 \times 10^{-5} M_\odot\,\mathrm{yr}^{-1}$ while Quataert's model varies from $\sim 1 - 3 \times 10^{-5} M_\odot\,\mathrm{yr}^{-1}$. The stagnation radius, the boundary where the flow is divided between inflowing and outflowing, for both models coincide in the interval $\sim 2 - 3''$. The close agreement in the accretion rate, stagnation radius, and the overall same trend in the profiles strengthens our confidence on our numerical formalism. With success of our formalism modeling stellar winds and stellar winds in the presence of a BH in a cluster, we are now ready to model the globular cluster G1 with its highly debated central IMBH.

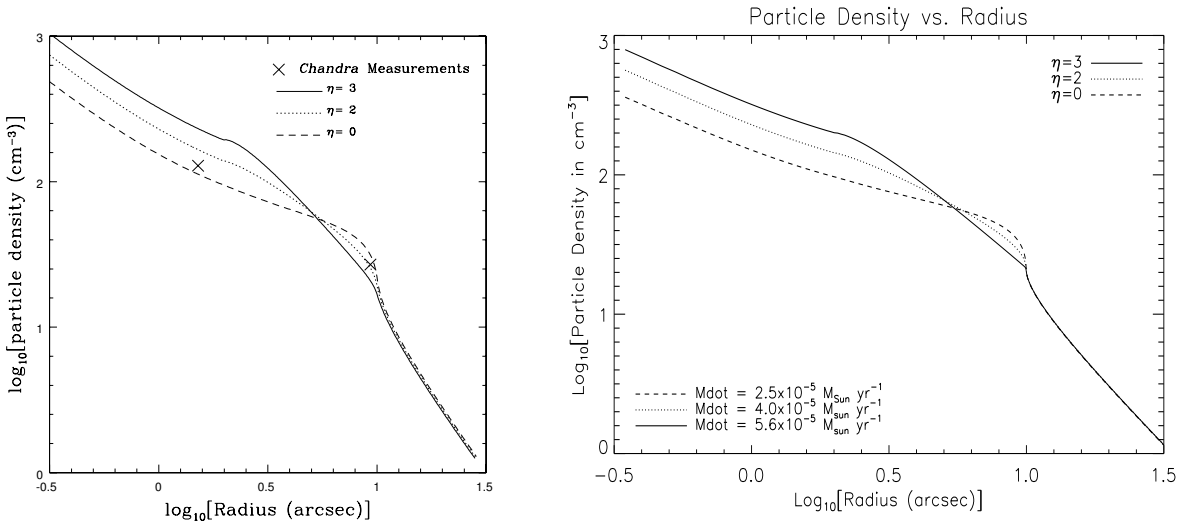

Figure 4.3: *Left panel*: *Particle density vs. radius* of the Galactic Center obtained by Quataert (2004). *Right panel*: *Particle density vs. radius* obtained by our numerical formalism. Both models predict same accretion rate $\sim 10^{-5} M_{\odot}\,\mathrm{yr}^{-1}$ for the three different η values.

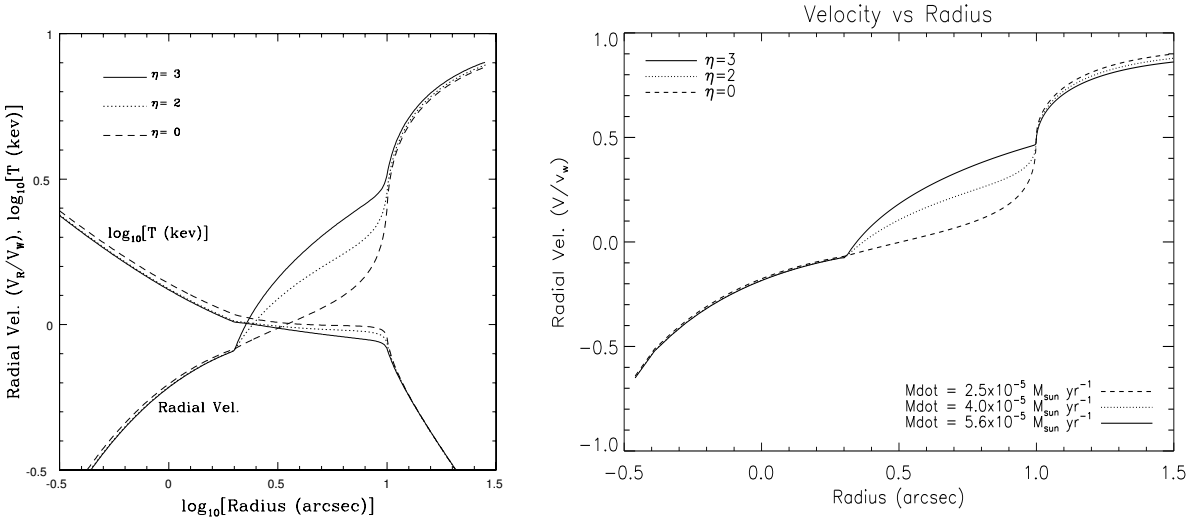

Figure 4.4: *Left panel*: *Velocity and Temperature vs. radius* of the Galactic Center obtained by Quataert (2004). *Right panel*: *Velocity vs. radius* obtained by our numerical formalism. The velocity profiles have the same trend and same corresponding stagnation radius $\sim 2{-}3''$.

4.0.3 G1

The globular cluster G1, in the Andromeda galaxy, has been suspected to harbor a central IMBH. Gebhardt et al. (2002) have calculated the mass to be $2^{+1.4}_{-0.8} \times 10^4 M_\odot$ derived from kinematic data from the Space Telescope Imaging Spectrograph on board the Hubble Space Telescope. This claim has been challenged by Baumgardt et al. (2003), which have shown that models without an IMBH are consistent with the data. The XMM-Newton X-ray observatory has conducted observations of G1 and discovered an X-ray source (see Figure 4.5), at a level of $L_{\rm x} \approx 2 \times 10^{36} {\rm erg\,s^{-1}}$, coincident with G1's nuclei (Trudolyubov & Priedhorsky 2004; Pooley & Rappaport 2006). The origin of the X-ray emission has been proposed by Pooley & Rappaport (2006) to be either accretion of ionized cluster gas by a central IMBH or a low mass X-ray binary. Either possible scenario cannot be discerned due to the inability of XMM-Newton to precisely localize the X-ray source.

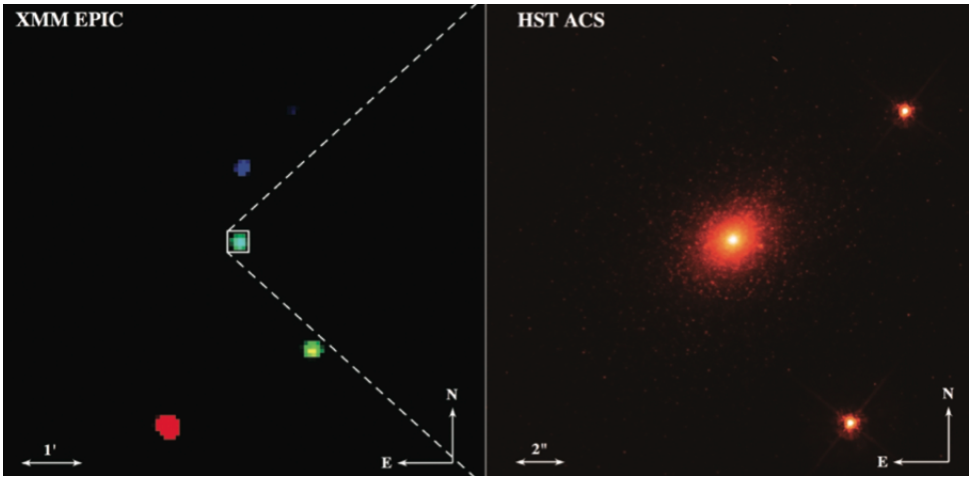

Figure 4.5: *Left panel*: XMM-Newton image of G1 with photons in the range of 0.5-1.2 keV shown in red, 1.2-2.5 keV shown in green, and 2.5-6 keV shown in blue. The small box indicates the area of the Hubble Space Telescope image on the right. *Right*: Hubble Space Telescope image G1.

With the formalism developed in this thesis we can attempt to model G1 with it's suspected central IMBH. Our values for $v_{\rm w}$ and $\dot{M}$ will be taken from the analysis of Pooley and Rappaport (2006). In their analysis they considered the evolution of stars near the turnoff mass (i.e., with $M \simeq 0.85 M_{\odot}$) to accurately represent the bulk of the stars in the cluster. To evolve the stars they used the evolution code by Soker & Rappaport (2000) and a modified wind-loss prescription by Reimers (1975). The evolution of the representative star cluster is taken from the zero age main sequence (ZAMS) to the asymptotic giant branch (AGB) phase. During the evolution the following integrals were tabulated

$$\Delta KE = \int_{\rm ZAMS}^{\rm AGB} \frac{1}{2} \dot{M} v_{\rm w}^2 \, dt \tag{4.28}$$

and

$$\Delta M = \int_{\rm ZAMS}^{\rm AGB} \dot{M} \, dt. \tag{4.29}$$

From the expressions above the mass-weighted mean specific kinetic energy

$$\frac{1}{2} \left\langle v_{\rm w}^2 \right\rangle \simeq \Delta KE / \Delta M \tag{4.30}$$

and the mean mass-loss rate from the winds

$$\langle \dot{M} \rangle \simeq \Delta M / \Delta t, \tag{4.31}$$

were computed, where Δt is the evolution time from the ZAMS to the end of the AGB phase. The calculations showed that $v_{\rm w} \simeq \sqrt{\langle v_{\rm w}^2 \rangle} \simeq 55 \, {\rm km \, s^{-1}}$ and $\dot{M} \simeq \langle \dot{M} \rangle \simeq 2 \times 10^{-11} M_{\odot} \, {\rm year}^{-1}$.

Having defined the properties of the emanating winds, we now need to specify the distribution of the stellar members inside the cluster. To this end, we use the Plummer (1911) functional form with parameters constrained from G1 observations. In the Plummer

model the density profile has the form

$$\rho(r) = \rho_0 \left(1 + \frac{r^2}{r_c^2}\right)^{-5/2} \tag{4.32}$$

where ρ_0 is the average density and r_c is the core radius. We use here the central density $4.7 \times 10^5 M_\odot\,\mathrm{pc}^{-1}$ and the core radius 0.52pc obtained by Meylan et al. (2001) from their observations with the Wide Field and Planetary Camera on board the Hubble Space Telescope. Since we are assuming the cluster to be comprised of stars at the turn off mass, then the number of stars enclosed by the radius per unit volume is

$$n(r) = \frac{\rho_0}{0.85 M_\odot} \left(1 + \frac{r^2}{r_c^2}\right)^{-5/2} \tag{4.33}$$

and therefore the stellar mass loss rate per unit volume is given by

$$q(r) = n(r)\dot{M} = \frac{\rho_0 \dot{M}}{0.85 M_\odot} \left(1 + \frac{r^2}{r_c^2}\right)^{-5/2}. \tag{4.34}$$

The effects of the gravitational force due to the stellar members as well the the IMBH can be incorporated on our model. From equation 4.32, the total mass of the stellar members enclosed by the radius r is written as

$$M_c(r) = \int_0^r \rho(r') 4\pi r^2 dr' = \frac{\rho_0 4\pi r_c^3}{3} \frac{r^3}{(r^2 + r_c^2)^{3/2}}, \tag{4.35}$$

hence, the total gravitational force per unit mass is

$$F(r) = \frac{-GM(r)}{r^2} = \frac{-G}{r^2} \left(\frac{\rho_0 4\pi r_c^3}{3} \frac{r^3}{(r^2 + r_c^2)^{3/2}} + M_{\mathrm{BH}}\right), \tag{4.36}$$

where M_{BH} is the mass of the IMBH. With all the essential ingredients in place, we can then proceed to simulate the stellar wind flow at the nuclei of G1.

Figures 4.6 and 4.7 show the density and velocity profiles for G1 for two cases. The first case (dashed line), considers only the gravitational potential of the IMBH. The

second (solid line), is the combined gravitational potential of the IMBH and the stellar members. The accretion rates onto the IMBH are $1.7 \times 10^{-7} M_{\odot}\,\mathrm{year}^{-1}$ for the first case and $6.5 \times 10^{-7} M_{\odot}\,\mathrm{year}^{-1}$ for the second case. The figures show, as we foreshadowed in section §3.2, that including the gravitational potential of the stellar members significantly increases the fraction of the gas retained which in turn increases the accretion rate onto the IMBH. The computed accretion rates are nonetheless relatively low when compared to the Eddington accretion rate: $\dot{M}_{\mathrm{edd}} = 0.016 M_{\odot}\,\mathrm{year}^{-1}$.

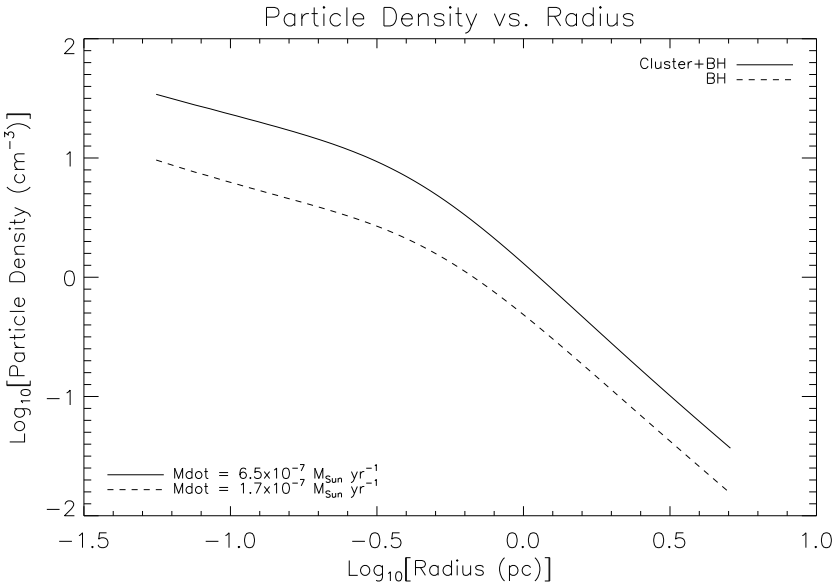

Figure 4.6: *Particle Density vs. Radius* for G1 and it suspected IMBH. A Plummer model was used for the density profile. The parameters used for the Plummer model where $\rho_0 = 4.7 \times 10^5 M_{\odot}\,\mathrm{pc}^{-1}$ and $r_{\mathrm{c}} = 0.52\,\mathrm{pc}$ considering the gravitational potential of the IMBH and the stellar members.

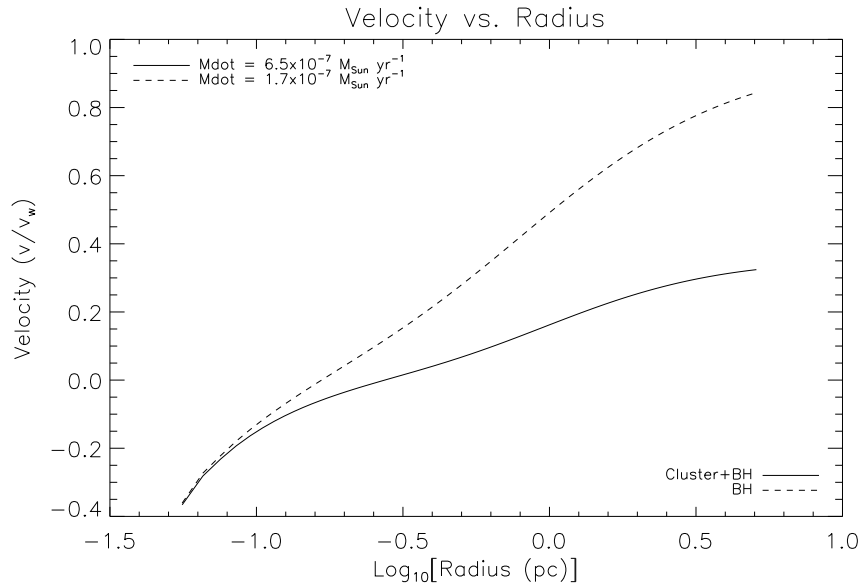

Figure 4.7: *Velocity vs. Radius* for G1 and it suspected IMBH. From the Plummer model and the analysis of Pooley, we were able to construct the mass loss rate per unit volume. The accretion rate onto the IMBH was $1.7 \times 10^{-7} M_{\odot}$ year^{-1} considering only the gravitation potential of the IMBH and $6.5 \times 10^{-7} M_{\odot}$ year^{-1}

For accretion rates much less than the Eddington rate, the gravitational potential energy released by turbulent stresses in an accretion flow near the black hole may be primarily stored as thermal energy, rather than being radiated away. In other words, radiation is dynamically unimportant and the inflow time of the gas can be significantly shorter than the cooling time. Such accretion flows are refer to as low-radiative accretion flows. For $\dot{m} = \dot{M}/\dot{M}_{\rm edd} \sim 10^{-4}$ (where $\dot{M}_{\rm edd}$ is the associated Eddington mass accretion rate, see Appendix B), the expected radiative efficiency is roughly $\eta \sim 10^{-3}$ (Quataert 2001) which gives a radiative luminosity of the order of 10^{36}erg s^{-1}, consistent with the luminosity observed at X-ray energies.

5

Discussion and Future Prospects

A numerical formalism able to accurately compute the feeding rates of MBHs due solely to the ingestion of winds from neighboring stars is developed in the preceding chapters. First, we have calculated the properties of the flow resulting from the interaction of the stellar winds emanating from stars belonging to a cluster or stellar cusp in the absence of a central MBH. The derived properties of the flow agree well with the analytic solutions, thus giving further credence to the validity of our numerical framework. Second, we have incorporated the gravitational potential of both the stellar members and the MBH in our model. This addition allowed us to compare our model of the Galactic Center with it's central SMBH with that derived by Quataert (2004). The solutions derived are in good agreement with Quataert's profiles, having the same accretion rates $\sim 10^{-5} M_{\odot}\,\mathrm{year}^{-1}$ and overall density, temperature, and velocity structures. Having successfully validated our numerical formalism, we use it to model, for the first time, the central regions of the globular cluster G1 with it's highly debated central IMBH. The radiative luminosity of G1, deduced by our analysis, is about $10^{36}\mathrm{erg\,s}^{-1}$, which is consistent with the observed radiative

luminosity. Our results provide further evidence to the idea that a central, moderately massive black hole resides in the core of G1. However, our formalism needs to be improved before a stronger case can be made. This is mainly because we have neglected the cooling properties of the inflowing gas and the black hole feedback processes, which we are in the process of implementing. The results of such improvements will be presented in an upcoming paper.

Although the numerical formalism presented here is simple it has far reaching applications. The ability to implement a stellar mass loss rate per unit volume and the gravitational potential for any given galactic nuclei or stellar cluster core self-consistently will provide us with an indispensable tool to understand the properties of these elusive MBHs.

Appendix A

General Relativity of Black Holes

In a nutshell the essence of Einsteins General Theory of Relativity is: Space acts on matter, telling it how to move. In turn, matter reacts back on space, telling it how to curve. For our case we will not need to dwell in General Relativity but we will need only one concept, the Schwarzschild Radius. The space-time geometry of a non-rotating star is encompassed in the metric

$$(ds^2) = \left(cdt\sqrt{1-2GM/rc^2}\right)^2 - \left(\frac{dr}{\sqrt{1-2GM/rc^2}}\right)^2 - (rd\theta)^2 - (r\sin\theta d\phi)^2 \qquad \text{(A.1)}$$

When the surface of the star collapses to the radial position

$$r_{\mathrm{s}} = \frac{2GM}{c^2}, \qquad \text{(A.2)}$$

known as the *Schwarzschild radius*, the square roots of the metric go to zero. At $r = r_{\mathrm{s}}$ the behavior of space and time have interesting consequences. For example the proper time is $d\tau = 0$, which means time has slowed to a complete stop, as measured from an observer at a large distance from the star.

Appendix B

Eddington Limit

We consider a steady spherically symmetrical accretion onto a compact object, say a black hole, which has mass M. Further we assume the accreting material be hydrogen which is fully ionized. Now there are generally two forces on the plasma, one is due to the inward pull of the gravitational force, and the second is due the outward force from the outflowing radiation. The radiation exerts a force mainly to the free electrons through Thomson scattering, since the cross section of the proton is a factor $(m_e/m_p)^2 \approx 3 \times 10^{-7}$ smaller, we can safely ignore it. Call S the radiant energy flux and σ_T the the Thomas cross section, then the outward force is $\sigma_T S/c$, where c is the speed of light. The radiative force pushes out the electrons which in turn push out the protons due to their coulomb attraction counteracting the pull of gravity. If the L is the luminosity of the accreting source, we have $S = L/4\pi r^2$ by spherical symmetry. Therefore the net force on the electron-proton pair is

$$F_{\text{net}} = \frac{L\sigma_T}{4\pi r^2 c} - \frac{GM(m_p + m_e)}{r^2} \cong \left(\frac{L\sigma_T}{4\pi c} - GMm_p\right)\frac{1}{r^2}. \tag{B.1}$$

The critical luminosity, when the forces balance, is known as the Eddington limit (or luminosity)

$$L_{\text{edd}} \equiv \frac{4\pi c G M m_p}{\sigma_T}. \tag{B.2}$$

Numerically the the Eddington limit is

$$L_{\text{edd}} \cong 1.3 \times 10^{38} \left(\frac{M}{M_\odot} \right) \text{erg s}^{-1}. \tag{B.3}$$

Additionally, the Eddington mass accretion rate is defined as

$$\dot{M}_{\text{edd}} \cong \frac{10 L_{\text{edd}}}{c^2}. \tag{B.4}$$

Appendix C

Hydrodynamics

In this section we derive the equations that describe the motion of a fluid. In order to describe the motion of a fluid, we must specify its properties at every point. For example, at any point in space at a specific moment in time the fluid will be moving with a specific velocity. Hence, to describe the velocity of the fluid we need to specify three components of velocity for each point in space at every moment in time. The equations that govern the dynamics of the fluid are based on the concepts of Newtonian mechanics, namely the conservation of mass, momentum and energy. Therefore at any arbitrary parcel of the fluid, we demand the parcel to obey the conservations laws stated above.

C.1 Conservation of Mass

Consider a fixed fluid parcel with volume V bound by a surface S. We ask: What is the rate at which the amount of mass in this volume is changing? At any moment in time

the amount of mass $m(t)$ in the volume V is

$$m(t) = \iiint_V \rho(\vec{r}, t)\, \mathrm{d}V, \tag{C.1}$$

where $\rho(\vec{r}, t)$ is the density of the fluid. The rate that the mass is changing is

$$\frac{dm}{dt} = \frac{d}{dt} \iiint_V \rho\, \mathrm{d}V = \iiint_V \frac{\partial \rho}{\partial t}\, \mathrm{d}V. \tag{C.2}$$

Now take an infinitesimally small surface patch of S and call it ΔS. Consider the total amount of mass Δm that passes through ΔS in a time Δt. Let $\hat{n}$ be the unit normal of the surface of ΔS and $\vec{v}$ be the velocity of fluid, so that in a time Δt a volume of $\vec{v}\,\Delta t \cdot \hat{n}\Delta S$ is swept out. Thus, the total amount of mass Δm that crosses through ΔS in a time Δt is simply the density times the volume,

$$\Delta m = \rho\, \vec{v}\, \Delta t \cdot \hat{n} \Delta S. \tag{C.3}$$

The mass per time passing through ΔS is $\rho\, \vec{v} \cdot \hat{n} \Delta S$. Hence, the mass gained by the volume V is equal to the integral of the normal component of the flow through all of the elements of the surface

$$- \oiint_S \rho\, \vec{v} \cdot \hat{n} \mathrm{d}S, \tag{C.4}$$

the negative sign is due to equation C.4 describes an outflow. Now since mass is conserved, it can never be lost or created, equation C.4 must be equal to equation C.2

$$\iiint_V \frac{\partial \rho}{\partial t}\, \mathrm{d}V = - \oiint_S \rho\, \vec{v} \cdot \hat{n} \mathrm{d}S. \tag{C.5}$$

Using Gauss Theorem we may convert a closed surface integral to a volume integral by means of the divergence operator. So equation C.5 may also be written as

$$\iiint_V \frac{\partial \rho}{\partial t}\, \mathrm{d}V = - \oiint_S \rho\, \vec{v} \cdot \hat{n} \mathrm{d}S = - \iiint_V \nabla \cdot (\rho\, \vec{v}) \mathrm{d}V \tag{C.6}$$

or

$$\iiint_V \left(\frac{\partial \rho}{\partial t} + \nabla \cdot (\rho \, \vec{v}) \right) \mathrm{d}V = 0. \tag{C.7}$$

Since this is true for all volumes, we can write

$$\frac{\partial \rho}{\partial t} + \nabla \cdot (\rho \, \vec{v}) = 0. \tag{C.8}$$

The above equation is the hydrodynamic equation of continuity. This is the first equation of three that we will derive. Foreshadowing latter derivations, it is useful to write equation C.8 in another form. Using the chain rule we can express the total time derivative d/dt as

$$\frac{d}{dt} = \frac{\partial}{\partial t} + \frac{dx}{dt}\frac{\partial}{\partial x} + \frac{dy}{dt}\frac{\partial}{\partial y} + \frac{dz}{dt}\frac{\partial}{\partial z} = \frac{\partial}{\partial t} + \vec{v} \cdot \nabla. \tag{C.9}$$

Further, from vector analysis we have the following identity

$$\nabla \cdot (\phi \vec{A}) = \vec{A} \cdot \nabla \phi + \phi \nabla \cdot \vec{A}. \tag{C.10}$$

Therefore the continuity equation can be written as

$$\frac{\partial \rho}{\partial t} + \vec{v} \cdot \nabla \rho + \rho \nabla \cdot \vec{v} = 0 \tag{C.11}$$

or

$$\frac{d\rho}{dt} + \rho \nabla \cdot \vec{v} = 0. \tag{C.12}$$

C.2 Momentum Equation

The momentum equation is derived by using Newton's law, which tells us how the momentum changes due to forces. Consider a parcel of the fluid with volume V and bounded by the surface S. The parcel experiences a force $-p \, \mathrm{d}\vec{S}$ due to the pressure acting on the surface patch $\mathrm{d}\vec{S}$. The negative sign arises because the surface patch vector is outwards, and

the force acting on the element is inwards. Now in general the force acting in the direction $\hat{n}$ is $-p\,\hat{n}\cdot \mathrm{d}\vec{S}$. Thus the net force acting over the whole parcels surface in the direction $\hat{n}$ is

$$F_n = -\oiint_S p\,\hat{n}\cdot \mathrm{d}\vec{S} = -\iiint_V \nabla\cdot(p\hat{n})\mathrm{d}V, \tag{C.13}$$

by Gauss' Theorem. In general the net force in the $\hat{n}$ direction is,

$$F_n = -\iiint_V \nabla\cdot(p\hat{n})\mathrm{d}V + \iiint_V \vec{f}\cdot\hat{n}\,\mathrm{d}V \tag{C.14}$$

where $\vec{f}$ is the net force per unit volume for the problem of interest, ie. gravitational, electromagnetic, radiation pressure, etc.

Following Newtons prescription, the time rate of change of the fluids momentum in the $\hat{n}$ direction is due to the applied forces

$$\left(\frac{d}{dt}\iiint_V \rho\,\vec{v}\,\mathrm{d}V\right)\cdot\hat{n} = -\iiint_V \nabla\cdot(p\,\hat{n})\,\mathrm{d}V + \iiint_V \vec{f}\cdot\hat{n}\,\mathrm{d}V. \tag{C.15}$$

Now notice

$$\nabla\cdot(p\hat{n}) = \hat{n}\cdot\nabla p + p\nabla\cdot\hat{n} = \hat{n}\cdot\nabla p, \tag{C.16}$$

since $\nabla\cdot\hat{n}$ is zero because $\hat{n}$ points at a constant direction. Now taking the limit when the fluid parcel becomes arbitrary small, we may replace the volume integral $\iiint_V \mathrm{d}V$ by ΔV, so then we have

$$\frac{d}{dt}(\rho\,\vec{v}\,\Delta V)\cdot\hat{n} = -\hat{n}\cdot\nabla p\,\Delta V + \vec{f}\cdot\hat{n}\,\Delta V. \tag{C.17}$$

or

$$\frac{d}{dt}(\rho\,\Delta V)\,\vec{v}\cdot\hat{n} + (\rho\,\Delta V)\frac{d\vec{v}}{dt}\cdot\hat{n} = -\Delta V\,\nabla p\cdot\hat{n} + \Delta V\,\vec{f}\cdot\hat{n}, \tag{C.18}$$

using the product rule on $\frac{d}{dt}(\rho\,\vec{v}\,\Delta V)$. The first term in equation C.18 is zero because we are riding with the fluid element and thus by mass conservation the mass in V is constant.

Thus we have

$$\left(\rho\frac{d\vec{v}}{dt} + \nabla p - \vec{f}\right) \cdot \hat{n}\, \Delta V = 0. \tag{C.19}$$

Since this must be true for all volumes and any arbitrary direction we arrive at

$$\rho\frac{d\vec{v}}{dt} = -\nabla p + \vec{f} \tag{C.20}$$

but using equation C.9 we finally have

$$\rho\frac{\partial\vec{v}}{\partial t} + \rho\,\vec{v}\cdot\nabla\,\vec{v} = -\nabla p + \vec{f}. \tag{C.21}$$

C.3 Energy Equation

The last and final equation we will derive is the energy equation. In an analogous way, our starting point is taking the dot product of the momentum equation with the velocity,

$$\vec{v}\cdot\left(\rho\frac{\partial\vec{v}}{\partial t} + \rho\,\vec{v}\cdot\nabla\,\vec{v}\right) = \vec{v}\cdot\left(-\nabla p + \vec{f}\right). \tag{C.22}$$

In Newtonian mechanics this is simply the rate at which energy is converted, $dE/dt = \vec{F}\cdot\vec{v}$. Making the use of the product rule

$$\frac{\partial\left(\rho\vec{v}\right)}{\partial t} = \frac{\partial\rho}{\partial t}\vec{v} + \rho\frac{\partial\vec{v}}{\partial t} \tag{C.23}$$

or rearranging terms

$$\rho\frac{\partial\vec{v}}{\partial t} = \frac{\partial\left(\rho\vec{v}\right)}{\partial t} - \frac{\partial\rho}{\partial t}\vec{v} = \frac{\partial\left(\rho\vec{v}\right)}{\partial t} + \left(\nabla\cdot\rho\vec{v}\right)\vec{v}, \tag{C.24}$$

where we have used the continuity equation $\partial\rho/\partial t + \nabla\cdot\left(\rho\,\vec{v}\right) = d\rho/dt + \rho\nabla\cdot\vec{v} = 0$ in the right hand side. Inserting equation C.24 into equation C.22 we have

$$\vec{v}\cdot\left(\frac{\partial\rho\vec{v}}{\partial t} + \left(\nabla\cdot\rho\vec{v}\right)\vec{v} + \rho\,\vec{v}\cdot\nabla\,\vec{v}\right) = \vec{v}\cdot\left(-\nabla p + \vec{f}\right). \tag{C.25}$$

From dyadic analysis we make use of the following identity

$$\nabla \cdot (\vec{A}\vec{B}) = (\nabla \cdot \vec{A})\vec{B} + \vec{A} \cdot (\nabla \vec{B}), \tag{C.26}$$

so applying the identity to $\rho\vec{v}\vec{v}$ it follows

$$\begin{aligned}
(\nabla \cdot \rho\vec{v})\vec{v} + \rho\vec{v} \cdot (\nabla\vec{v}) &= \nabla \cdot (\rho\vec{v}\vec{v}) && \text{(C.27)}\\
&= \nabla \cdot (\vec{v}\rho\vec{v}) && \text{(C.28)}\\
&= (\nabla \cdot \vec{v})\rho\vec{v} + \vec{v} \cdot (\nabla\rho\vec{v}) && \text{(C.29)}\\
&= (\vec{v} \cdot \nabla)\rho\vec{v} + \rho\vec{v}\,(\nabla \cdot \vec{v}). && \text{(C.30)}
\end{aligned}$$

The energy equation is now

$$\begin{aligned}
\vec{v} \cdot \left(\frac{\partial\,(\rho\vec{v})}{\partial t} + (\nabla \cdot \vec{v})\rho\vec{v} + \rho\vec{v}(\nabla \cdot \vec{v}) \right) &= \vec{v} \cdot \left(-\nabla p + \vec{f} \right) && \text{(C.31)}\\
\vec{v} \cdot \left(\frac{d\,(\rho\vec{v})}{dt} + \rho\vec{v}(\nabla \cdot \vec{v}) \right) &= \vec{v} \cdot \left(-\nabla p + \vec{f} \right) && \text{(C.32)}\\
\vec{v} \cdot \frac{d\,(\rho\vec{v})}{dt} + \rho v^2(\nabla \cdot \vec{v}) &= \vec{v} \cdot \left(-\nabla p + \vec{f} \right). && \text{(C.33)}
\end{aligned}$$

Now we examine the first term in equation C.33, where we use the Einstein convention (repeated index means summation in the three spatial dimension).

$$\begin{aligned}
\vec{v} \cdot \frac{d\,(\rho\vec{v})}{dt} &= v_k \frac{d\,(\rho v_k)}{dt} && \text{(C.34)}\\
&= v_k \frac{d\rho}{dt} v_k + v_k \rho \frac{dv_k}{dt} && \text{(C.35)}\\
&= v_k v_k \frac{d\rho}{dt} + \frac{1}{2}\,\rho \frac{d\,(v_k v_k)}{dt} && \text{(C.36)}\\
&= \frac{d}{dt}(\frac{1}{2}\rho v_k v_k) + \frac{1}{2} v_k v_k \frac{d\rho}{dt} && \text{(C.37)}\\
&= \frac{d}{dt}(\frac{1}{2}\rho v^2) - \frac{1}{2}\rho v^2(\nabla \cdot \vec{v}), && \text{(C.38)}
\end{aligned}$$

where in the manipulation we have used the product rule for $\frac{d}{dt}(\frac{1}{2}\rho v_k v_k)$ and the continuity equation. So the energy equation now has the form

$$\frac{d}{dt}(\frac{1}{2}\rho v^2) - \frac{1}{2}\rho v^2(\nabla \cdot \vec{v}) = \vec{v} \cdot \left(-\nabla p + \vec{f}\right). \tag{C.39}$$

Up to this point we have only considered the energy due to the moition of the fluid but the fluid also has internal energy governed by thermodynamics. Each parcel contains an amount of internal energy $\rho\epsilon$, where ϵ is the internal energy per unit mass. From the first law of thermodynamics, the change of internal energy is related to the work done by the unit mass of fluid and the heat absorbed by the unit mass from its surroundings

$$\Delta\epsilon = T\Delta s - p\Delta V, \tag{C.40}$$

where T is the temperature, s the entropy per unit mass, p the pressure, and V the volume occupied by a unit mass. Dividing by Δt and taking the limit as Δt goes to zero we have

$$\frac{d\epsilon}{dt} = T\frac{ds}{dt} - p\frac{dV}{dt} \tag{C.41}$$

$$\frac{d\epsilon}{dt} = T\frac{ds}{dt} - p\frac{d}{dt}\left(\frac{1}{\rho}\right) \tag{C.42}$$

$$\frac{d\epsilon}{dt} = T\frac{ds}{dt} + \frac{p}{\rho^2}\frac{d\rho}{dt}. \tag{C.43}$$

Differentiating $\rho\epsilon$ it follows

$$\frac{d\left(\rho\epsilon\right)}{dt} = \rho\frac{d\epsilon}{dt} + \epsilon\frac{d\rho}{dt} \tag{C.44}$$

$$\frac{d\left(\rho\epsilon\right)}{dt} = \rho\left(T\frac{ds}{dt} + \frac{p}{\rho^2}\frac{d\rho}{dt}\right) + \epsilon\frac{d\rho}{dt} \tag{C.45}$$

$$\frac{d\left(\rho\epsilon\right)}{dt} = \rho\frac{ds}{dt} + \left(\epsilon + \frac{p}{\rho}\right)\frac{d\rho}{dt} \tag{C.46}$$

$$\frac{d\left(\rho\epsilon\right)}{dt} = \rho\frac{ds}{dt} - \left(\rho\epsilon + p\right)\nabla \cdot \vec{v} \tag{C.47}$$

where we have used equation C.43 and the continuity equation. After rearranging terms we are left with

$$\frac{d\left(\rho\epsilon\right)}{dt} + \rho\epsilon\nabla\cdot\vec{v} = \rho\frac{ds}{dt} - p\nabla\cdot\vec{v}. \tag{C.48}$$

Adding equation C.48 with C.39 we have

$$\frac{d}{dt}\left[\rho\left(\frac{1}{2}v^2+\epsilon\right)\right] + \rho\left(\frac{1}{2}v^2+\epsilon\right)\nabla\cdot\vec{v} = -\vec{v}\cdot\nabla p - p(\nabla\cdot\vec{v}) + \vec{v}\cdot\vec{f} + \rho T\frac{ds}{dt} \tag{C.49}$$

Making use of identities C.9 and C.10 equation C.49 can be manipulated to

$$\frac{\partial}{\partial t}\left[\left(\frac{1}{2}\rho v^2+\epsilon\right)\right] + \nabla\cdot\left[\left(\frac{1}{2}\rho v^2+\rho\epsilon+p\right)\vec{v}\right] = \rho T\frac{ds}{dt} + \vec{v}\cdot\vec{f}. \tag{C.50}$$

This concludes our derivation for the equations of motion for a fluid. In summary we derived the following equations

$$\frac{\partial\rho}{\partial t} + \nabla\cdot\left(\rho\,\vec{v}\right) = 0 \qquad \text{(Continuity eq.)} \tag{C.51}$$

$$\rho\frac{\partial\vec{v}}{\partial t} + \rho\,\vec{v}\cdot\nabla\,\vec{v} = -\nabla p + \vec{f} \qquad \text{(Momentum eq.)} \tag{C.52}$$

$$\frac{\partial}{\partial t}\left[\left(\frac{1}{2}\rho v^2+\epsilon\right)\right] + \nabla\cdot\left[\left(\frac{1}{2}\rho v^2+\rho\epsilon+p\right)\vec{v}\right] = \rho T\frac{ds}{dt} + \vec{v}\cdot\vec{f} \qquad \text{(Energy eq.)} \tag{C.53}$$

Appendix D

Sound Waves in a Medium

We now develop the theory of wave propagation in an uniform medium. A compressible fluid can support small oscillations which we call sound waves. Sounds waves lead to a natural time-scale, usually referred as as the sound crossing-time, that allows us to assess if a region has time to dynamically respond to a disturbance before its affect by some other process in question.

We begin our analysis by studying a fluid in equilibrium and with the absence of external forces. Although our example is quite simple, the outline can be applied to many other circumstances. For our model the fluid equations (see C.51 – 53) will emit solutions of uniform density ρ_0, pressure p_0, and zero velocity $\vec{v} = 0$. We consider a small perturbations about the equilibrium

$$p = p_0 + p'(\vec{r}, t) \tag{D.1}$$

$$\rho = \rho_0 + \rho'(\vec{r}, t) \tag{D.2}$$

$$\vec{v} = \vec{v}', \tag{D.3}$$

where the primed quantities are assumed to small respectively to their equilibrium counterpart. Substituting the perturbations equations into the continuity and momentum equations and neglecting second and higher order products of them we have

$$\frac{\partial}{\partial t}(\rho_0+\rho') + \nabla\cdot\left[(\rho_0+\rho')\vec{v}'\right] = 0 \qquad \text{(Continuity Equation)} \tag{D.4}$$

$$\frac{\partial}{\partial t}(\rho') + \rho_0\nabla\cdot\vec{v}' = 0 \tag{D.5}$$

$$(\rho_0+\rho')\left[\frac{\partial\vec{v}'}{\partial t} + \vec{v}'\cdot\nabla\vec{v}'\right] = \nabla(p_0+p') \qquad \text{(Momentum Equation)} \tag{D.6}$$

$$\rho_0\frac{\partial\vec{v}'}{\partial t} = -\nabla p' \tag{D.7}$$

For the energy equation, we suppose the perturbations are adiabatic or isothermal so we can replace the energy equation by $p = K\rho^\gamma$. Thus, substituting the perturbations it follows

$$(p'+p_0) = K(\rho_0+\rho')^\gamma = K\rho_0^\gamma(1+\frac{\rho'}{\rho_0})^\gamma \tag{D.8}$$

$$\approx K\rho_0^\gamma(1+\gamma\frac{\rho'}{\rho_0}) = p_0 + \gamma\frac{p_0\rho'}{\rho_0} \tag{D.9}$$

or

$$p' = \left(\frac{dp}{d\rho}\right)_0\rho', \tag{D.10}$$

where $(dp/d\rho)_0 = dp_0/d\rho_0$ is the derivative evaluated at the equilibrium. Thus, equation D.7 becomes

$$\rho_0\frac{\partial\vec{v}'}{\partial t} = -\left(\frac{dp}{d\rho}\right)_0\nabla\rho' \tag{D.11}$$

We eliminate $\vec{v}'$ from D.5 and D.7 by operating with $\partial/\partial t$ and $\nabla\cdot$ respectively and noting that $[\partial/\partial t, \partial/\partial x_k] = 0$ and then subtracting we finally arrive to

$$\frac{\partial^2\rho'}{\partial t^2} = \left(\frac{dp}{d\rho}\right)_0\nabla^2\rho' \tag{D.12}$$

Equation D.12 is the well known *wave equation* with sound speed

$$c_s = \sqrt{\left(\frac{dp}{d\rho}\right)_0}. \tag{D.13}$$

Appendix E

Abbreviation Used

AGN	Active Galactic Nuclei
AMR	Adaptive Mesh Refinement
BH	Black Hole
IMBH	Intermediate Mass Black Hole
MBH	Massive Black Hole
PPM	Piecewise Parabolic Method
SMBH	Super Massive Black Hole
ULX	Ultra Luminous X-ray Source

Bibliography

Barnes, J. E., & Hernquist, L. 1992, ARA&A, 30, 705

Baumgardt, H., Makino, J., Hut, P., McMillan, S., & Portegies Zwart, S. 2003, ApJL, 589, L25

Bondi, H. 1952, MNRAS, 112, 195

Cantó, J., Raga, A. C., & Rodríguez, L. F. 2000, ApJ, 536, 896

Di Matteo, T., Springel, V., & Hernquist, L. 2005, Nature, 433, 604

Ferrarese, L., & Ford, H. 2005, SSR, 116, 523

Fryxell, B., et al. 2000, ApJS, 131, 273

Gebhardt, K., Rich, R. M., & Ho, L. C. 2002, ApJL, 578, L41

Genzel, R., Eckart, A., Ott, T., & Eisenhauer, F. 1997, MNRAS, 291, 219

Gerssen, J., van der Marel, R. P., Gebhardt, K., Guhathakurta, P., Peterson, R. C., & Pryor, C. 2002, AJ, 124, 3270

—. 2003, AJ, 125, 376

Hernquist, L. 1989, Nature, 340, 687

Ho, L., Kormendy, J., & Murdin, P. 2000, Supermassive Black Holes in Active Galactic Nuclei, ed. Murdin, P.

Kormendy, J., Ho, L., & Murdin, P. 2001, Supermassive Black Holes in Inactive Galaxies, ed. Murdin, P.

Kormendy, J., & Richstone, D. 1995, ARA&A, 33, 581

Krabbe, A., Genzel, R., Drapatz, S., & Rotaciuc, V. 1991, ApJL, 382, L19

Landau, L. D., & Lifshitz, E. M. 1959, Fluid mechanics, ed. Landau, L. D. & Lifshitz, E. M.

Löhner, R. 1987, Computer Methods in Applied Mechanics and Engineering, 61, 323

Magorrian, J., et al. 1998, AJ, 115, 2285

Melia, F. 2009, High-Energy Astrophysics, ed. Melia, F.

Meylan, G., Sarajedini, A., Jablonka, P., Djorgovski, S. G., Bridges, T., & Rich, R. M. 2001, AJ, 122, 830

Najarro, F., Krabbe, A., Genzel, R., Lutz, D., Kudritzki, R. P., & Hillier, D. J. 1997, AAP, 325, 700

Plummer, H. C. 1911, MNRAS, 71, 460

Pooley, D., & Rappaport, S. 2006, ApJL, 644, L45

Portegies Zwart, S. F., Baumgardt, H., Hut, P., Makino, J., & McMillan, S. L. W. 2004, Nature, 428, 724

Quataert, E. 2001, in Astronomical Society of the Pacific Conference Series, Vol. 224, Probing the Physics of Active Galactic Nuclei, ed. B. M. Peterson, R. W. Pogge, & R. S. Polidan, 71–+

Quataert, E. 2004, ApJ, 613, 322

Soker, N., & Rappaport, S. 2000, ApJ, 538, 241

Soltan, A. 1982, MNRAS, 200, 115

Thorne, K. S. 1994, Priroda, 11, 87

Trudolyubov, S., & Priedhorsky, W. 2004, ApJ, 616, 821

Yu, Q., & Tremaine, S. 2002, MNRAS, 335, 965

Zezas, A., Fabbiano, G., Rots, A. H., & Murray, S. S. 2002, ApJ, 577, 710